Master's Thesis

Spin-controlled Nonlinear Harmonic Generations from Polaritonic Metasurface

Kim. Daeik

Department of Electrical Engineering

Graduate School of UNIST

2020

Spin-controlled Nonlinear Harmonic Generations from Polaritonic Metasurface

Kim. Daeik

Department of Electrical Engineering

Graduate School of UNIST

Spin-controlled Nonlinear Harmonic Generations from Polaritonic Metasurface

A thesis/dissertation
submitted to the Graduate School of UNIST
in partial fulfillment of the
requirements for the degree of
Master of Science

Daeik Kim

2019.12.02 of submission
Approved by

_____

Advisor
Jongwon Lee

Spin-controlled Nonlinear Harmonic Generations from Polaritonic Metasurface

Daeik Kim

This certifies that the thesis/dissertation of Daeik Kim
is approved.

2019.12.02 of submission

signature

_____

Advisor: Jongwon Lee

signature

_____

typed name: Joo-Yun Jung

signature

_____

typed name: Jiwon Chang

Abstract

Metasurfaces have shown new possibilities to develop various applications, such as nonlinear holography, nonlinear wave mixing, and novel nonlinear light sources. In nonlinear optics, nonlinear harmonic generation from nonlinear metasurface provide a new degree-of-freedom. Nonlinear metasurfaces have various interesting properties, such as the relaxed phase matching constraints, efficient frequency mixing, and nonlinear local phase control. There are many studies on the nonlinear metasurfaces, but the development of a single nonlinear metasurface platform having giant nonlinear responses and single nonlinear beam generation is still needed to develop for practical applications. In this thesis, I design, simulate, and experimentally demonstrate a novel class of a nonlinear polaritonic metasurface platform using nanoantenna structures with three- or four-fold rotational symmetry and multiple quantum well structures with giant 2^{nd} and 3^{rd} order nonlinear responses. Using the metasurface, spin-controlled giant 2^{nd} and 3^{rd} order nonlinear responses can be generated simultaneously or selectively on the same chip. Furthermore, under a circular polarized beam condition, nonlinear local phases can be simply tuned continuously by changing the rotation angle of the meta-atom based on the Pancharatnam-Berry phase. Based on continuous local nonlinear phase control, nonlinear beam-steering that maintain spin-controlled giant nonlinear response for the second- and third-harmonic generations, was experimentally demonstrated via gradient nonlinear polaritonic metasurfaces. The nonlinear metasurface platform that proposed in this study can be used to develop future practical applications such as nonlinear light source, nonlinear holography, and nonlinear multiplexing-based communications.

Contents

List of Figures - - -

LIST OF FIGURES

LIST OF Tables

I. Introduction

1.1 Surface Plasmon Polaritons

Surface Plasmon Polaritons (SPPs) are electromagnetic surface wave that travel along the metal-dielectric interface as shown in Figure 1.1.1 (a). They are a type of evanescently confined surface wave that is guided along the interface and only exist with Transverse Magnetic (TM) polarization.

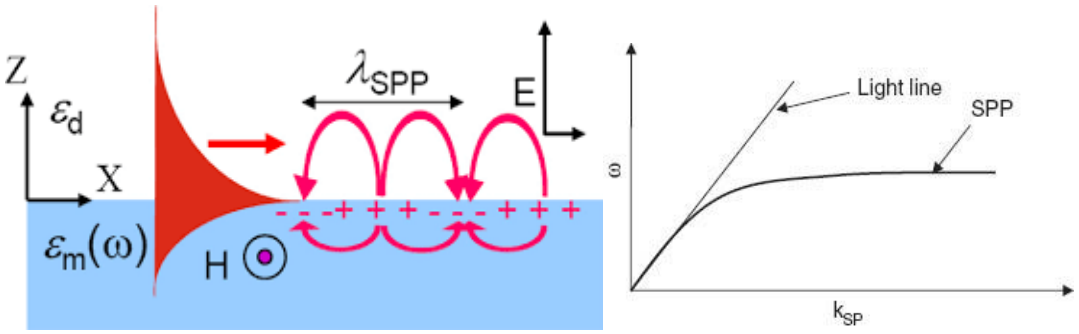

Figure 1.1.1. Schematic of (a) process of surface plasmonic polaritons (SPP) and (b) dispersion relation of SPP. [1]

Due to the TM field components are continuous across the metal-dielectric interface, the SPP magnetic field and magnetic electric field can be written as follows[1]

$$\overrightarrow{H_d}(z>0) = (0, H_{yd}, 0)e^{i(k_{SPP}x-wt)}\exp(-z\sqrt{k_{SPP}^2-\varepsilon_d k_0^2})$$

$$\overrightarrow{E_d}(z>0) = (E_{xd}, 0, E_{zd})e^{i(k_{SPP}x-wt)}\exp(-z\sqrt{k_{SPP}^2-\varepsilon_d k_0^2}) \quad (1.1.1)$$

$$\overrightarrow{H_m}(z<0) = (0, H_{ym}, 0)e^{i(k_{SPP}x-wt)}\exp(-z\sqrt{k_{SPP}^2-\varepsilon_d k_0^2})$$

$$\overrightarrow{E_m}(z<0) = (E_{xm}, 0, E_{zm})e^{i(k_{SPP}x-wt)}\exp(-z\sqrt{k_{SPP}^2-\varepsilon_d k_0^2}) \quad (1.1.2)$$

where H_{yd} and $H_{yd(m)}$ are the amplitude of the magnetic field components in the dielectric and metal medium E_{xd} and E_{zd} are the amplitude of the electric field components in the dielectric and metal

medium, ε_m and ε_d are permittivities of dielectric and metal, k_0 is the light wavenumber and $k_{SPP} = k_x$.

Applying the boundary condition for normal electric and magnetic-field components, $\varepsilon_m E_{zm} = \varepsilon_d E_{zd} E_{xm} = E_{xd} H_{ym} = H_{yd}$, the SPP dispersion relation can be written as

$$k_{spp} = \frac{\omega}{c}\sqrt{\frac{\varepsilon_m \varepsilon_d}{\varepsilon_m + \varepsilon_d}} \tag{1.1.3}$$

where c indicates the speed of light, ω indicates angular frequency. The required condition for the existence of SPP can be determined from the square root expressions of Eq. (1.1.3) and to have a positive real part, as follow $Re\{\varepsilon_m(\omega)\} < -\varepsilon_d$ equation is needed. This requirement is met in the long-wavelength part of the infrared and visible for most metals and dielectrics. The SPP wavelength is determined by real part of the propagation constant ($\lambda_{spp} = 2\pi/Re(k_{SPP})$) ,which is determined by the real part of the propagation constant. λ_{spp} is always much shorter than the light wavelength in the dielectric ($\lambda = \lambda_0/\sqrt{\varepsilon_d}$) and the SPP propagation length ($L_{SPP} = 1/Im(2k_{SPP})$).[2-3] Figure 1.1.1 (b) shows light and SPP dispersion plots at interface on a metal using the loss-less Drude model. The SPP wavelength reaches to nearly zero at the short wavelength limit of the SPP dispersion when $\omega \rightarrow \omega_p/\sqrt{1+\varepsilon_d}$. When $\varepsilon_m(\omega) + \varepsilon_d = 0$ is satisfied, the corresponding limiting frequency of SPPs is called surface plasmons (SPs).

1.2 Intersubband Transitions from Quantized Energy Band in MQW

Intersubband transition (IST) from multi-quantum-well structures are electron transitions between quantized energy bands in the conduction band states that generated by quantum confinement in nano-thickness of semiconductor layers.[4] Electrons can be confined in one-direction in the conduction band and the allowed energy levels that are determined by the relative band offsets of the two or three semiconductor materials, are quantized along the growth direction. The transition energy can be adjusted by changing the doping level, width and depth of the quantum well. An intersubband transition can be generated only when the multi quantum well (MQW) is doped so that charge carriers of a single type are existed (electrons in n-doped case). Figure 1.2.1 (a) shows intersubband and interband transition in a n-doped quantum well. Figure 1.2.1 (b) shows the joint density of states (JDOS) of intersubband and interband transition in a MQW. In case of intersubband transition, JDOS has a narrow

single peak which leads to strong resonant absorption when the incident photon is polarized in the growth (z) direction.[5]

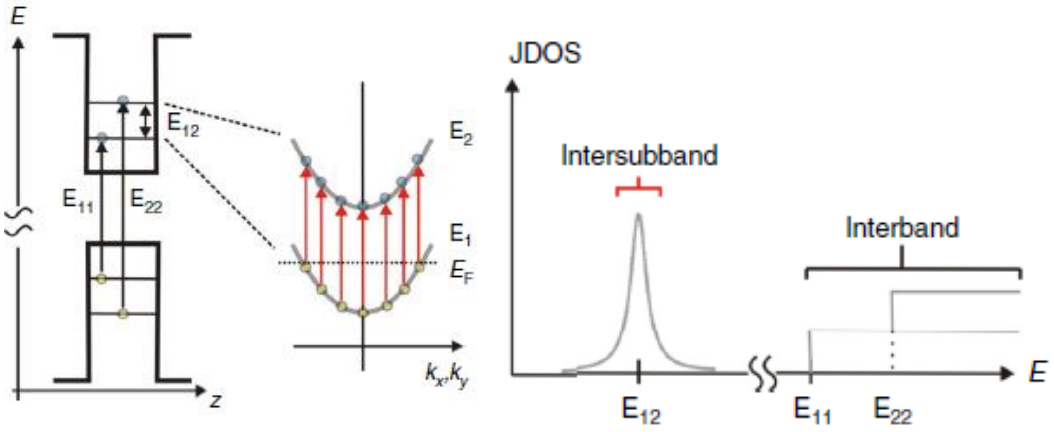

Figure 1.2.1. (a) Intersubband (E_{12}) and interband (E_{11} and E_{22}) transition in a n-doped quantum well. (b) Joint density of states (JDOS) for intersubband and interband transition in a n-doped quantum well. [5]

It is known since the late 1980s, researchers studied and demonstrated the n-doped coupled MQWs to obtain giant both second order nonlinear susceptibilities and third order nonlinear susceptibilities ($\chi^{(2)}, \chi^{(3)}$, respectively) The magnitude of nonlinear susceptibilities up to 10^4 to 10^5 times greater than traditional bulk nonlinear materials such as silicon.[6] Using these giant nonlinear susceptibilities, various nonlinear optical processes such as second harmonic generation (SHG)[7-9], third harmonic generation (THG)[10], optical rectification, optical phase conjugation and other four-wave mixing process are studied.[11-13] The basic design approach to engineering electron subband, is based on tailoring the composition and widths of wells and barrier in MQW structure. Using this approach, the quantum mechanical expression for $\chi^{(2)}$ or $\chi^{(3)}$ for nonlinear process by adjusting dipole moments and energy level positions.

In a resonant four-level system, the quantum mechanical expression for the second- and third-order nonlinear susceptibility terms are simply expressed when the pump frequencies are close to intersubband resonances and the resonant term is dominant. For SHG, 2nd nonlinear susceptibility can be written as[14]

$$\chi^{(2)}_{zzz}(\omega \to 2\omega) = N_e \frac{e^3}{\varepsilon_0 h^2} \frac{z_{12} z_{23} z_{31}}{(\omega - \omega_{12} - i\gamma_{12})(2\omega - \omega_{13} - i\gamma_{13})} \quad (1.2.1)$$

and for THG, 3rd nonlinear susceptibility can be written as[10]

$$\chi^{(3)}_{zzzz}(\omega \to 3\omega) = N_e \frac{e^4}{\varepsilon_0 \hbar^3} \frac{z_{12}z_{23}z_{34}z_{41}}{(\omega-\omega_{12}-i\gamma_{12})(2\omega-\omega_{13}-i\gamma_{13})(3\omega-\omega_{14}-i\gamma_{14})} \tag{1.2.2}$$

where ω indicates the input frequency, N_e indicates the average bulk doping density, e indicates the electron charge, $\hbar\omega_{ij}$ is transition energy, $\hbar\Upsilon_{ij}$ is transition linewidth and z_{ij} is dipole moment between energy states i and j.

1.3 Nonlinear Photonic metasurface

In nonlinear optics, the nonlinear optical response of a nonlinear material can be expressed by a power series expansion of nonlinear material polarization as follow

$$P^{NL} = \varepsilon_0(\chi^{(2)}E^2 + \chi^{(3)}E^3 + \ldots\chi^{(n)}E^n) \tag{1.3.1}$$

where respectively, $\chi^{(2)}$ and $\chi^{(3)}$ indicate the second-order and third-order nonlinear susceptibilities, respectively, E indecates the electric field and ε_0 is permittivity of vacuum.[15] In nonlinear photonics, duo to the mixing of the pumping wave, the nonlinear material polarization acts as a source for new frequency. Figure 1.3.1 shows general nonlinear optical mechanisms. 2nd harmonic generation and 3rd harmonic generation are nonlinear optical processes that two or three photons with the same angular frequency ω interact with a nonlinear material, are combined to create a single photon with angular frequency 2 ω and 3 ω respectively. FWM is a third order nonlinear optical process in which three fundamental photons interact with a nonlinear material and then new frequency of light is generated.

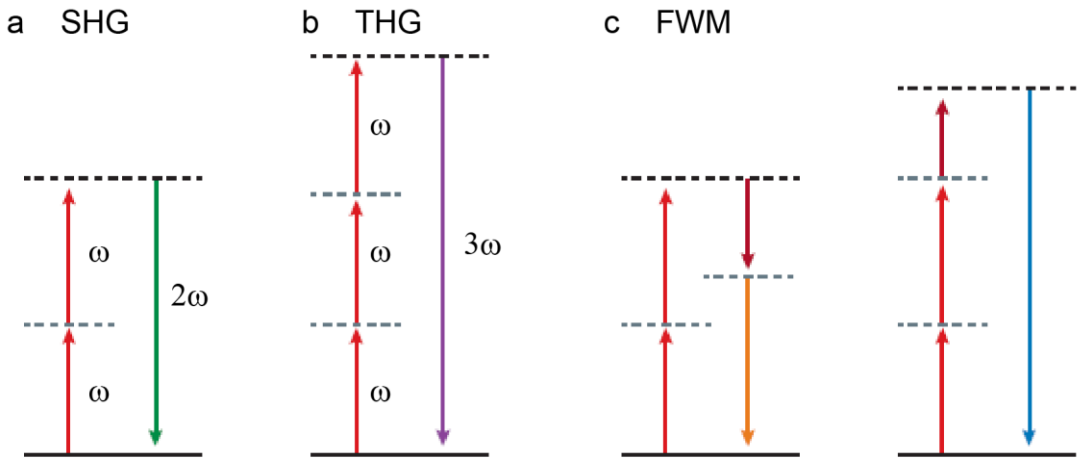

Figure 1.3.1. Schematic of nonlinear optical processes. The solid and dashed line mean electronic energy level and the arrow line represent energy transition. (a) energy diagrams of Second harmonic generation (SHG), (b) Third harmonic generation (THG) and (c) nondegenerate four-wave-mixing (FWM). [15]

In nonlinear optical process, usually, phase matching conditions are crucial for harmonic generations and FWM[16-20]. Recently, metasurfaces which have thicknesses of the order of subwavelengths, have greatly interested owing to their ability for greatly relaxing phase-matching constraints.[21-22] In linear optics, at circularly polarized incident wave condition, the meta-atoms that based on the Pancharatnam-Berry (PB) phase are capable of continuous 2π phase simply tuning by changing the rotation angle of meta-atom.[23-27] Moreover, in nonlinear optics, a new design method has been studied to continuously control the phase of harmonic generation by applying the PB phase elements. Nonlinear photonic metasurfaces have greatly attracted owing to their ability to control the local amplitude, phase of the nonlinear response using PB phase at subwavelength scale.[28-33] As shown in Figure 1.3.2, by employing the PB phase approach, various nonlinear applications, such as nonlinear diffraction, nonlinear OAM generation, and nonlinear holography and imaging have been demonstrated.[1, 34-35]

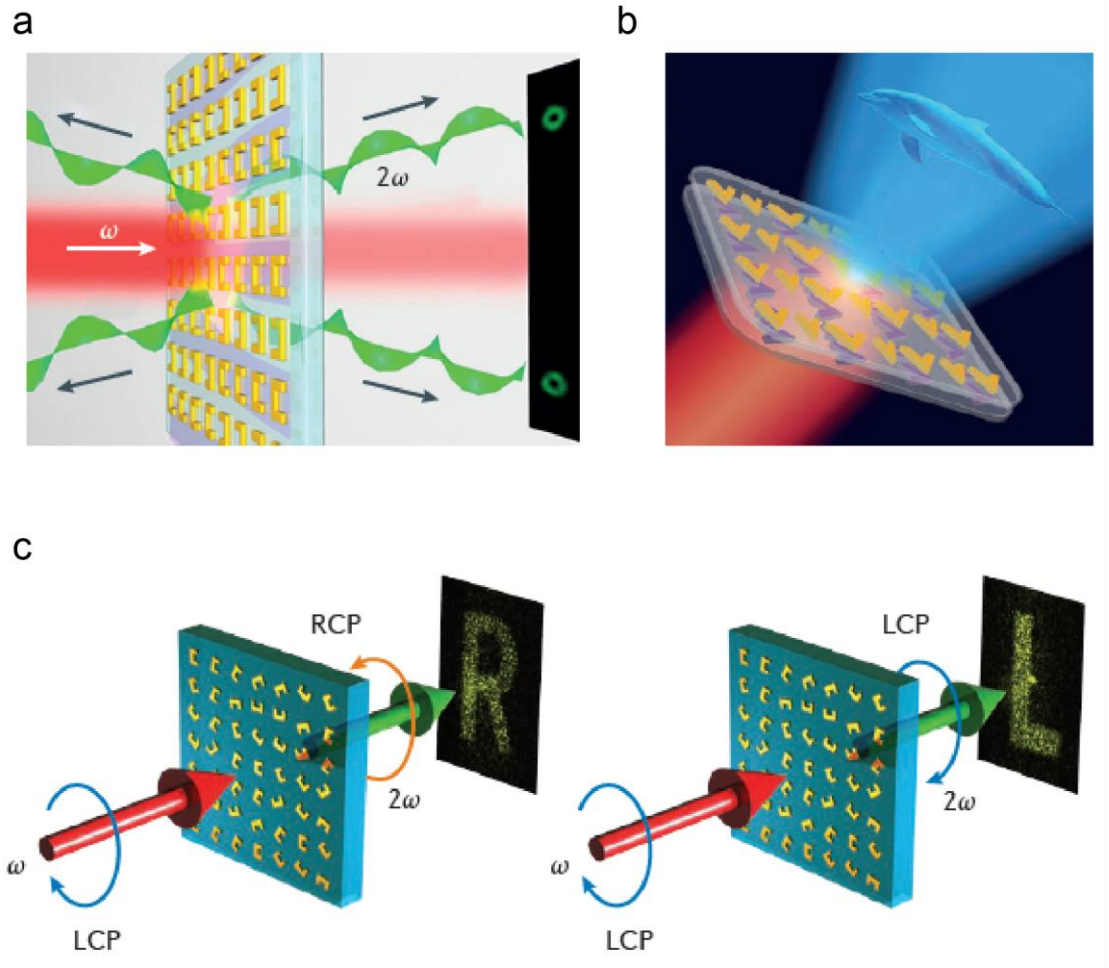

Figure 1.3.2. Applications of nonlinear photonic metasurfaces. (a) Diffraction of nonlinear harmonic generated signal from metasurface. (b) Nonlinear harmonic generation hologram using metasurface. (c) Nonlinear hologram for circularly polarized incident beam with nonlinear metasurface. [15]

1.4 Spin Angular Momentum Control

In linear optical PB phase, the phase factor at circular polarized incident beam, express as $e^{i2\phi\sigma}$ where ϕ is rotation angle of meta-atom and σ is '+' or '-' sign that indicate to spin-state of the light (Right circular polarization (RCP) and left circular polarization (LCP), respectively).[27, 36] Such a PB phase in the nonlinear material polarization can be understood in a coordinate transformation process. After transforming, the expression of the nonlinear dipole moment is

$$\mathrm{P}_{\theta,\sigma}^{n\omega} = \mathrm{P}_{\theta,L,\sigma}^{n\omega} e^{-i\sigma\theta} \propto e^{(n-1)i\sigma\theta} \tag{1.4.1}$$

$$\mathrm{P}_{\theta,-\sigma}^{n\omega} = \mathrm{P}_{\theta,L,-\sigma}^{n\omega} e^{i\sigma\theta} \propto e^{(n+1)i\sigma\theta} \tag{1.4.2}$$

The nonlinear polarizabilities of the plasmonic antenna can be written as

$$\alpha_{\theta,\sigma,\sigma}^{n\omega} \propto e^{(n-1)i\sigma\theta} \tag{1.4.3}$$

$$\alpha_{\theta,-\sigma,\sigma}^{n\omega} \propto e^{(n+1)i\sigma\theta} \tag{1.4.4}$$

where ω indicates the angular frequency of input pump beam, n present *n*th harmonic generation, ϕ is rotation angle of plasmonic antenna, σ and - σ are the circular polarization states and L is the plasmonic antenna's local coordinate frame.[37] Therefore, the geometry phase of the *n*th harmonic generation is expressed as $(n-1)\sigma\theta$ or $(n+1)\sigma\theta$ with the equal or opposite circular polarization regarding to the input pump, respectively. As shown in Figure 1.4.1, according to the selection rules at circular polarized input pump beam, only harmonic orders of $n = lm \pm 1$ are allowed with a single meta-atom structure with *m*-fold rotational symmetry, where l is an integer and the + sign or – sign indicate to spin-state of the nonlinear signal. The + sign is the same as the circular polarization of the input pump and – sign is the opposite of circular polarization of input pump.[38-41]

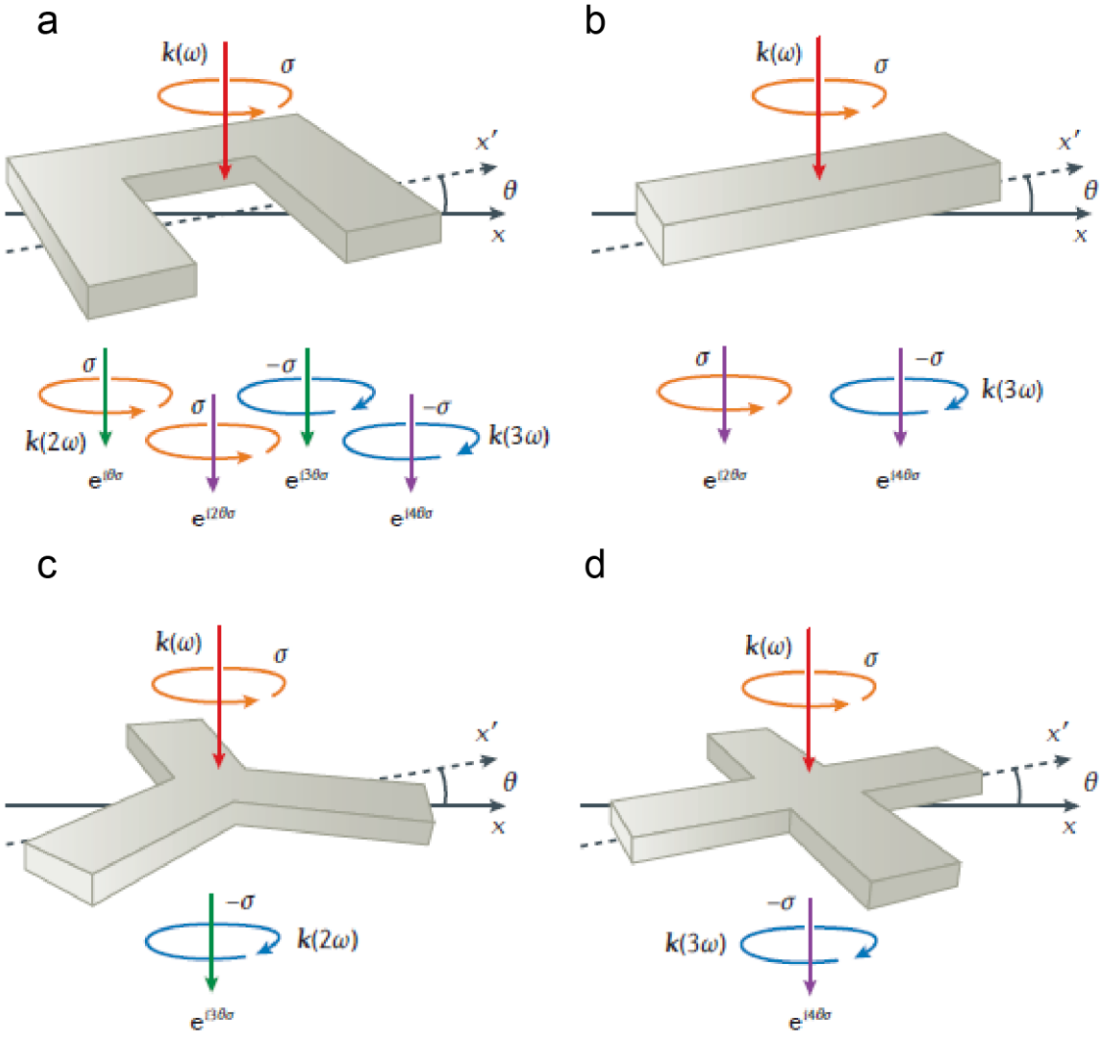

Figure 1.4.1. Nonlinear PB phase elements with CP pump. (a) Phases of the nonlinear harmonic waves that generated from a $C1$ (1-fold symmetry) plasmonic antenna. (b) Phases of the nonlinear harmonic waves that generated from a $C2$ (2-fold symmetry) plasmonic antenna. (c) Phases of the nonlinear harmonic waves that generated from a $C3$ (3-fold symmetry) plasmonic antenna. (d) Phases of the nonlinear harmonic waves that generated from a $C4$ (4-fold symmetry) plasmonic antenna. [15]

Therefore, by choosing a meta-atom with m-fold ($m \geq 3$) rotational symmetry, we can control the spin-state of the nonlinear signal (Figure 1.4.2).

Harmonic order	Sign of σ	C_1	C_2	C_3	C_4
$n=1$	+				
	−	$2\theta\sigma$	$2\theta\sigma$		
$n=2$	+	$\theta\sigma$			
	−	$3\theta\sigma$		$3\theta\sigma$	
$n=3$	+	$2\theta\sigma$	$2\theta\sigma$		
	−	$4\theta\sigma$	$4\theta\sigma$		$4\theta\sigma$
$n=4$	+	$3\theta\sigma$		$3\theta\sigma$	
	−	$5\theta\sigma$			
$n=5$	+	$4\theta\sigma$	$4\theta\sigma$		$4\theta\sigma$
	−	$6\theta\sigma$	$6\theta\sigma$	$6\theta\sigma$	

Figure 1.4.2. The order of the nonlinear process and the rotational symmetry meta-atoms (C1 to C4) determine the phase of the nonlinear wave during the harmonic generation processes. n represent a harmonic order, θ is rotation angle of meta-atom and σ is spin-state (circular polarization) of the light. [15]

1.5 Overview of the Thesis

In this thesis, I experimentally demonstrate a nonlinear polaritonic metasurface that obtains spin controlled SHG and THG on one-chip system based on combining a MQW layer using a coupled three quantum well system with plasmonic nanostructure.

In Chapter 2, I designed three- and four-fold (C3 and C4) rotational symmetry meta-atom to control the spin-state of the nonlinear signal from harmonic generation and to achieve a giant nonlinear response both SHG and THG, respectively. By using geometric phase, the metasurface that can continuous local phase control of the SHG and THG nonlinear beam was demonstrated.

In Chapter 3, I designed to nonlinear chiral meta atom with C3 and C4 structure for circular dichroism in nonlinear signal (SHG and THG, respectively).

II. Spin-controlled Nonlinear Harmonic Generations

2.1 Introduction

In linear optics, a metasurface that is based on the arrangement of meta-atoms with subwavelength scale, owing to its ability to control the local phase and amplitude, has opened opportunities for new types of flat optics that can replace conventional, bulky optical components.[42-43] In nonlinear optics, a metasurface also have greatly attracted due to their capacity to achieve various frequency conversion or mixing effects with greatly relaxed phase-matching constraints and ability to control the local phase, amplitude, and polarization of the nonlinear response. Recently, to continuously control the local phase and amplitude of nonlinear response, a new design method that applying the PB phase elements, has been studied. Various nonlinear applications, like nonlinear OAM generation, nonlinear beam-steering, and nonlinear holography and imaging have been demonstrated by employing the PB phase approach.[15, 28-29, 31-32] However, as I mentioned in introduction part(1.2, 1.3, 1.4), there have still issues and challenges about the nonlinear metasurface.

In this chapter, I experimentally demonstrate a nonlinear polaritonic metasurface to produce spin controlled SHG and THG simultaneously or selectively, on one-chip system by combining the MQW layer using a coupled three quantum well and plasmonic nano-cavity structure. The meta atoms that occur plasmonic nano-cavity, are designed to have three- and four-fold (C3 and C4) rotational symmetry for SHG and THG, respectively. In this case, three important characteristics can be achieved simultaneously: (i) giant nonlinear responses, (ii) precise spin-state control of the nonlinear beam, and (iii) continuous local phase control of the SHG and THG nonlinear beam.

2.2 Design of Nonlinear Metasurface

2.2.1 Design of MQW and Metasurface

The 400 nm-thick MQW layer which was designed to have giant 2nd and 3rd order nonlinear susceptibilities, was used as a nonlinear medium. As shown in Figure 2.2.1. the MQW was constructed by repeating the single period of an $In_{0.53}Ga_{0.47}As/Al_{0.48}In_{0.52}As$ coupled three quantum well structure. The layer sequence of the quantum well was 4/**4.6**/1.2/**2**/1.2/**1.8**/4 (in nanometers), where the boldface listings represent the $In_{0.53}Ga_{0.47}As$ well layer. I doped to 4×10^{18} cm^{-3} at the first well (4.6 nm). The

widths of the quantum wells are designed to induce four electron subbands in the coupled three quantum wells that can generate the giant 2nd and 3rd order nonlinear susceptibilities. $\chi^{(2)}_{zzz}$ and $\chi^{(3)}_{zzzz}$ were occurred by the electron transitions that were polarized in the direction perpendicular to the surface (z-direction) among the 1st, 2nd, 3rd levels, or among the 1st, 2nd, 3rd, and 4th levels, respectively.

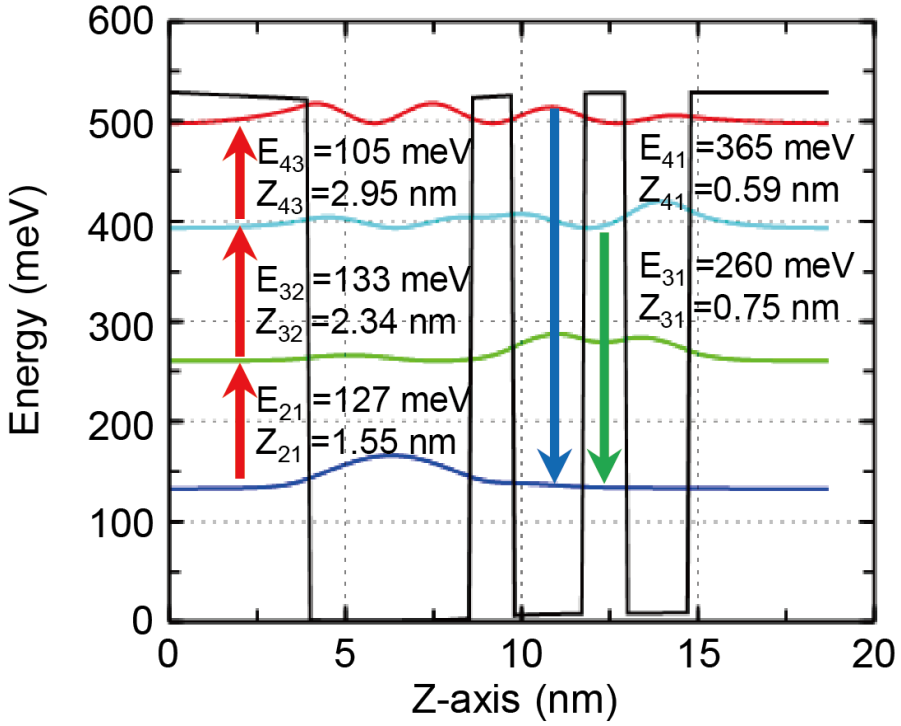

Figure 2.2.1. One period of conduction band diagram of the MQW with $In_{0.53}Ga_{0.47}As/Al_{0.48}In_{0.52}As$ coupled three-quantum-well structure designed for giant 2nd and 3rd order nonlinear responses. Z_{ij} and E_{ij} Z_{ij} are the dipole moment element and transition energy of the intersubband transitions between electron subbands i and j, respectively.

By using the MQW structure that is coupled with plasmonic nanoantenna, it can simultaneously use the giant 2nd and 3rd order nonlinear responses and can selectively or simultaneously generate coherent SHG or THG in the far-field. Figure 2.2.2 a and b show the $\chi^{(2)}_{zzz}$ and $\chi^{(3)}_{zzzz}$ values that were calculated by numerical calculation using the physical parameters extracted from the intersubband absorption measurement. $\chi^{(2)}_{zzz}$ and $\chi^{(3)}_{zzzz}$ have maximum values of 171 nm V^{-1} and 2.27×10^{-14} m^2 V^{-2} near the 10.5 μm wavelength. The SH and TH peak intensity I_{2w} and I_{3w}, respectively can be expressed as[10, 44]

$$I_{2w} = \frac{4}{8}\omega^2\eta_0^3\left(\varepsilon_0\chi_{ijk}^{(2)eff}\right)^2 I_\omega^2 L^2$$

(2.1.1)

$$I_{3w} = \frac{9}{16}\omega^2\eta_0^4\left(\varepsilon_0\chi_{ijkl}^{(3)eff}\right)^2 I_\omega^3 L^2$$

(2.1.2)

where ω indicates the input frequency, η_0 is $1/\varepsilon_0 c$, ε_0 is the permittivity in a vacuum, c indicates the speed of light in a vacuum, I_ω indicates intensity of the input beam, L indicates the MQW layer thickness and χ^{eff} is effective nonlinear susceptibility expressed as[10, 44]

$$\chi_{RRR(LLL)}^{(2)eff} = \chi_{zzz}^{(2)}\left[\int_{V_{MQW}} \xi_{R(L)}^{2\omega}(x,y,z)\xi_{R(L)}^{\omega}(x,y,z)\xi_{R(L)}^{\omega}(x,y,z)dV\right]/V_{unit}$$

(2.1.3)

$$\chi_{RRRR(LLLL)}^{(3)eff} = \chi_{zzzz}^{(3)}\left[\int_{V_{MQW}} \xi_{R(L)}^{3\omega}(x,y,z)\xi_{R(L)}^{\omega}(x,y,z)\xi_{R(L)}^{\omega}(x,y,z)\xi_{R(L)}^{\omega}(x,y,z)dV\right]/V_{unit}$$

(2.1.4)

where $\xi_{R(L)}^{\omega}, \xi_{R(L)}^{2\omega}, \xi_{R(L)}^{3\omega}$ are the respective local E_z-field enhancements in the MQW normalized to the incident E-field with the RCP (LCP) spin state at the frequencies of $\omega, 2\omega, 3\omega$. V_{unit} and V_{MQW} are the volumes of the MQW region of the meta-atom before and after etching, respectively. And overlap factor is expressed as $\chi_{RRR(LLL)}^{(2)eff}/\chi_{zzz}^{(2)}$ and $\chi_{RRRR(LLLL)}^{(3)eff}/\chi_{zzzz}^{(3)}$ for SHG and THG, respectively. Therefore, if higher overlap factor is achieved, the effective 2nd and 3rd order nonlinear susceptibility can be increased and also increased the SH and TH peak intensity.

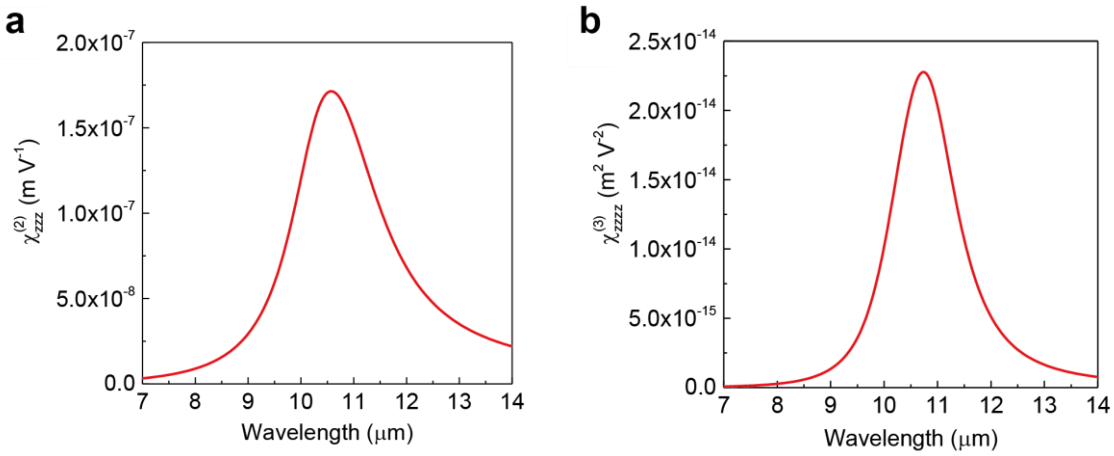

Figure 2.2.2. Nonlinear susceptibilities of the MQW structure as a function of the input pump wavelength (a) second order nonlinear susceptibility for SHG. (b) third order nonlinear susceptibility for THG

As I mentioned in introduction part, under the circular polarization (CP) input pump, the spin state of nonlinear signal generated from the metasurface with certain rotational symmetry is limited by the selection rule. Therefore, to realize the spin-controlled nonlinear harmonic generations, I designed C3 and C4 meta-atom structures which is combined with a MQW layer which was sandwiched between a bottom metallic backplane and the top Au nanoantenna, for SHG and THG, respectively. Figure 2.2.3 a and 1b show unit cell schematics of the C3 and C4 meta-atom for SHG and THG, respectively.

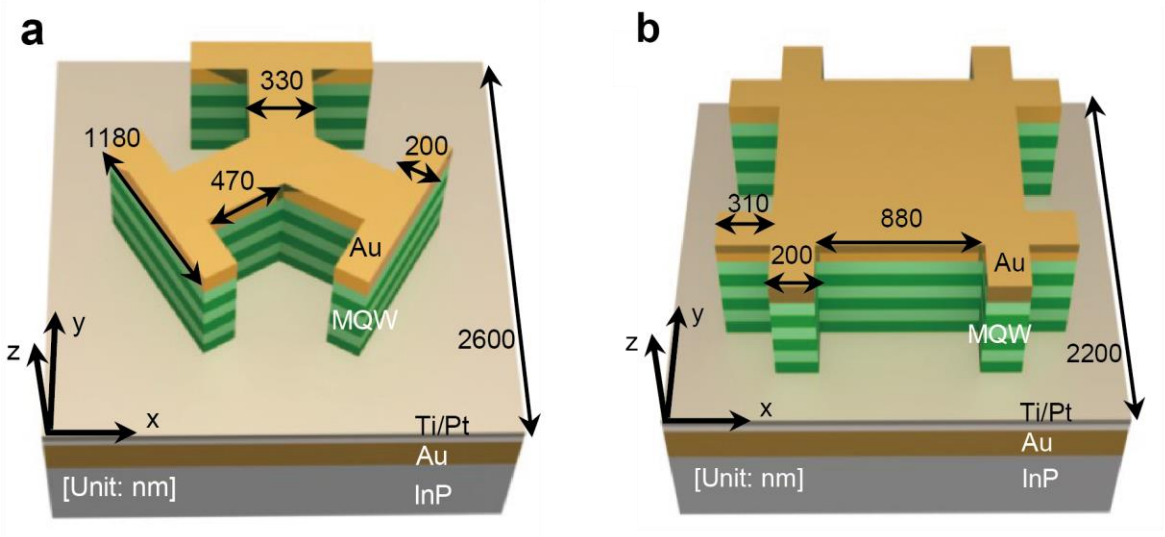

Figure 2.2.3. Schematics of meta-atom designs. (a) Unit cell structure of the plasmonic antenna with C3 rotational symmetry designed for SHG. (b) Unit cell structure of the plasmonic antenna with C4 rotational symmetry designed for THG.

2.2.2 Simulation and Calculation of Nonlinear Response

For numerical calculations and simulations, I used numerical code and commercial Finite-Difference Time-Domain solver (Matlab and Lumerical FDTD Solutions (ver. 8.19), respectively). In FDTD simulation, periodic boundary condition in the x- and y-direction and perfectly matched layer (PML)

boundary condition in the z-direction were used. The gold layers that used as bottom metal and plasmonic nano antenna, were modeled as Drude metal with collision frequency of $\Gamma = 1.224 \times 10^{14}\mathrm{rad/s}$ and plasma frequency of $\omega_p = 1.378 \times 10^{16}\mathrm{rad/s}\Gamma = 1.224 \times 10^{14}\mathrm{rad/s}$. For the MQW layer, I used the in-plane and out-of-plane dielectric constants that are calculated from the absorption measurement and parameter calculations. Figure 2.2.4 shows the E_z field enhancement distributions with normalized incident circularly polarized E-field. The E_z field enhancement distributions that were induced in MQW layer, were monitored at the 100 nm below the top Au nanoantenna. Figure 2.2.4 a and b show the normalized E_z-field enhancement distribution induced in the meta-atom with 3-fold rotational symmetry, at fundamental frequency (FF, λ_{FF} ~10.5 μm) and second harmonic (SH, λ_{SH} ~5.2 μm) frequency, respectively. And Figure S2 c and d show the normalized E_z-field enhancement distribution induced in the meta-atom with 4-fold rotational symmetry, at FF and third harmonic (TH, λ_{TH} ~3.5 μm) frequency, respectively. The E_z-field enhancement was confirmed that more than 3 times at FF, SH, and TH frequency in the MQW layer.

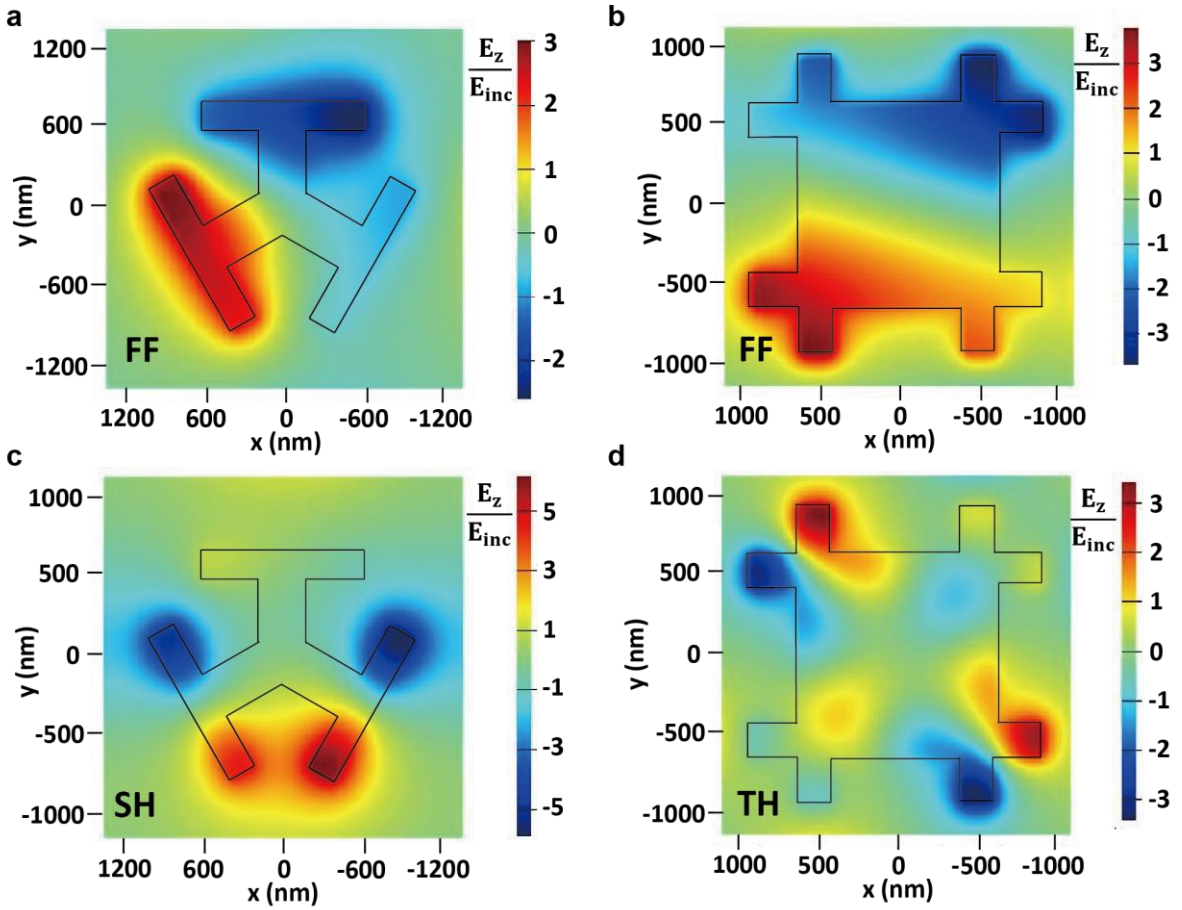

Figure 2.2.4. The normalized E_z field distribution on the plasmonic meta-atom. The E_z field monitor is in MQW layer. Top-view cross-section at the (a) FF and (b) SH frequency for the C3 meta-atom and at the (c) FF and (d) TH frequency for the C4 meta-atom.

Figure 2.2.5 a and b show linear absorption characteristics of the two metasurfaces for SHG and THG, respectively. Linear absorption characteristics were simulated and experimentally measured using a Finite-Difference Time-Domain solver and a Fourier Transform Infrared (FTIR) spectrometer equipped, respectively. The Fourier Transform Infrared (FTIR) spectrometer consist of an IR microscope was used and an unpolarized broadband IR light was used as an input source. As shown in Figure 2.2.5, C3 and C4 structure have strong absorption peaks near the FF (λ_{FF} ~ 10.5 μm), and each harmonic frequency (SH frequency, λ_{SH} ~ 5.2 μm and the TH frequency, λ_{TH} ~ 3.5 μm for C3 and C4, respectively. The measured absorption results and simulation results were well matched.

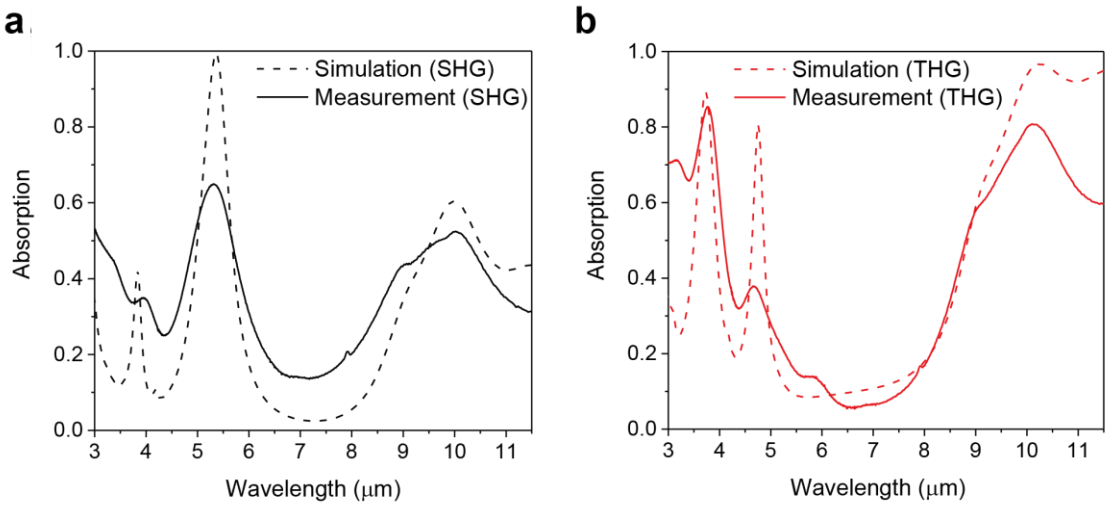

Figure 2.2.5. Simulation and experiment results of linear absorption spectra of the nonlinear metasurface for SHG (C3 structure) (a) and THG (C4 structure) (b).

2.3 Fabrication

Figure 2.3.1 indicates the fabrication step of the nonlinear metasurface. The MQW layers were grown on the InP substrate via metal-organic chemical vapor deposition (MOCVD). The layers were grown on the InP substrate in the following order: first etch stop layer of $In_{0.53}Ga_{0.47}As$ (300 nm thick), second etch stop layer of InP (100 nm thick) and the MQW layers. A 10 nm thick layer of titanium was evaporated on top of the MQW as an adhesion layer, a 50 nm thick layer of platinum was sequentially evaporated as an Au diffusion blocking layer and a 200 nm thick layer of Au was evaporated on top of the layer, sequentially. The MQW (InP substrate) wafer was bonded with a GaAs wafer by thermal bonding. The InP substrate and $In_{0.53}Ga_{0.47}As$ layer were removed by selective wet etching via chemical solution. As shown in Figure 2.3.1 c, a 5nm thick layer of titanium as an adhesion layer, and a 50nm thick of Au for nano-resonator, were evaporated on the MQW layer. A 430 nm thick of silicon nitride (SiN_x) layer was deposited by plasma-enhanced chemical vapor (PECVD) for mask layer. The e-beam resist was coated on the silicon nitride layer and nano-resonator arrays were patterned on the silicon nitride layer by electron beam lithography. After the e-beam lithography, nano-resonator arrays were patterned on SiN layer by inductively coupled plasma (ICP) etching. The metal layer and MQW layer were etched by inductively coupled plasma (ICP) etching and SiN make was removed by wet etching using buffered oxide etchant (BOE).

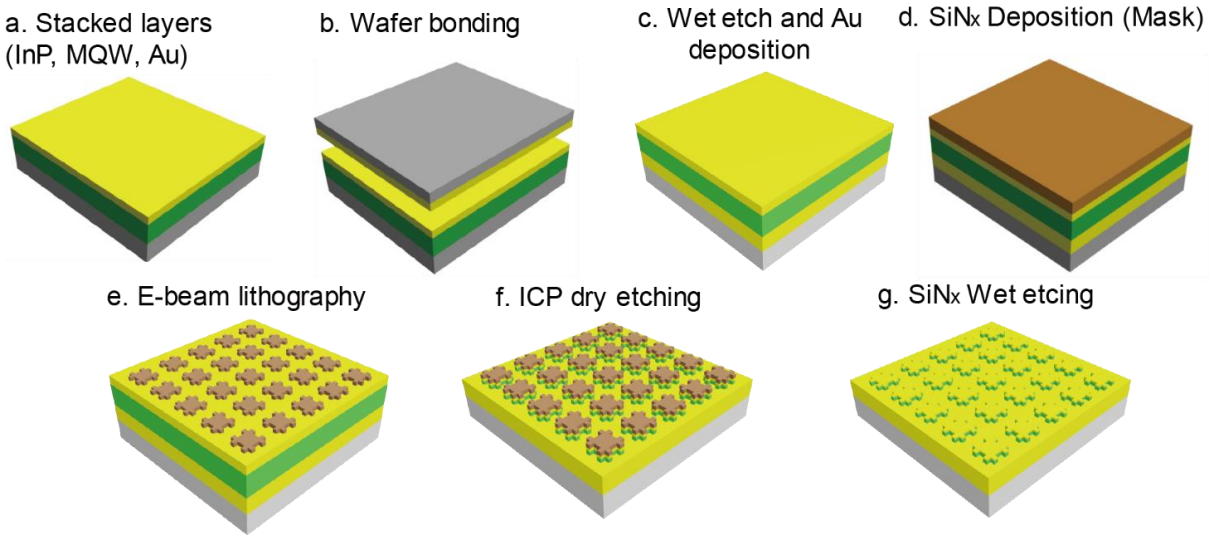

Figure 2.3.1. Schematic of fabrication step of the nonlinear metasurface.

Epi-layer design and growth

The multi quantum well structure for giant nonlinear susceptibility was designed via a self-consistent Poisson-Schrodinger solver. In this case, I used a particular composition of two materials, $In_{0.53}Ga_{0.47}As$ / $Al_{0.48}In_{0.52}As$, in which the lattice constants of the layers are virtually matched well to that of InP substrate. The growth sheet of the MQW layers is shown in Table 2.3.1. In this case, I used Molecular-Beam Epitaxy (MBE) for growing the MQW layers.

Layer	**Material**	**[nm]**	**Ratio**	**Doping (cm^{-3})**
1	InGaAs	300	$In_{0.53}Ga_{0.47}As$	
2	InP	100		
3	AlInAs	4	$Al_{0.48}In_{0.52}As$	
Start of 7 repeat periods				
4	AlInAs	4	$Al_{0.48}In_{0.52}As$	
5	InGaAs	4.6	$In_{0.53}Ga_{0.47}As$	4×10^{18}
6	AlInAs	1.2	$Al_{0.48}In_{0.52}As$	
7	InGaAs	2	$In_{0.53}Ga_{0.47}As$	
8	AlInAs	1.2	$Al_{0.48}In_{0.52}As$	
9	InGaAs	1.8	$In_{0.53}Ga_{0.47}As$	
10	AlInAs	4	$Al_{0.48}In_{0.52}As$	
End of repeat periods				
11	AlInAs	4	$Al_{0.48}In_{0.52}As$	

Table 2.3.1. Growth sheet for MQW epi-layer. The InP substrate was used as substrate for growing the MQW layer.

Wafer bonding

In our case, gold-gold thermo-compression wafer bonding was used for MQW layer transfer onto a metal ground plane. For improving adhesion of metal layers onto the wafer and removing oxidation layer, the MQW wafer was cleaned by Reactive Ion Etching (RIE) ((FAB star, O_2 100sccm, 40mTorr, RF 100W, for 60sec) and by putting in BOE (buffered oxide etchant) for 10 seconds. The metal layers with 10nm of titanium, 50nm of platinum, and 150nm of gold were evaporated on the MQW layer and

GaAs wafer (Bare GaAs). The titanium layer is an adhesion layer and platinum layer is a metal diffusion blocking layer. The two wafers are placed and aligned on the bonding plate and a carbon sheet is placed on the parts. The bonding chamber is evacuated and pressure of the chamber is 1 kN/cm^2 and heated to 240°C. When the plates reached target temperature, 612 kgf (~6 kN) of clamping force was applied for 15minutes. After the bonding process, the plates were cooled down with force maintained and after cooling, the bonded sample is checked.

Substrate removal

After the wafer bonding, the InP substrate, layer and In0.53Ga0.47As layer were removed via selective wet etching. For InP layer, I use a HCl : deionized (DI) water = 3 : 1 as a wet etching solution. For In0.53Ga0.47As layer, I use a H_3PO_4 : H_2O_2 : DI water = 1 : 1 : 19 as a wet etching solution. Firstly, InP substrate was etched by mechanical polishing and for mechanical polishing, SiC gel is used. The initial thickness of sample is recorded and 150~200 μm-thick substrate is thin down via mechanical polishing. After the mechanical polishing, the remaining InP substrate was etched by HCl : DI water solution (InP etch rate : ~10μm/min, etch stop at In0.53Ga0.47As layer) until the etch stop layer (In0.53Ga0.47As layer). Secondly, In0.53Ga0.47As layer was removed by H_3PO_4 : H_2O_2 : DI water solution (In0.53Ga0.47As etch rate: ~2nm/sec, etch stop at InP layer) until etch stop layer (InP layer). And finally, InP layer was removed by HCl : DI water solution for a few seconds until surface color turns uniform.

Electron beam lithography and ICP etching

After wet etching, for removing surface oxidation and improve adhesion of metal layer, the MQW layer was cleaned by oxygen RIE (FAB star, O_2 100sccm, 40mTorr, RF 100W, for 60sec). To make a nano-resonator array, 5nm thick layer of titanium for adhesion layer and a 50nm thick of Au for nano-resonator, were evaporated on the MQW layer. After the metal deposition, a 430 nm thick of silicon nitride (SiN_x) layer was deposited by plasma-enhanced chemical vapor (PECVD, PEH-600, Heat delay: Temperature 350°C, N_2 100sccm, for 300sec, Gas flow: SiH_4 220sccm, NH_3 50sccm, for 60sec Process step: RF 60W for 450 sec) for mask layer. For electron beam lithography, AR-P-6200.09 is spin coated on the sample with 3000rpm for 1min and pre-baked at 150°C for 1min and double spin coated with 3000rpm for 1min and baked at 150°C for 2min. Designed nano-resonator arrays are patterned electron beam lithography machine (NB3, current 0.74Na, voltage 80keV, Dose 1.3C/m^2). After e-beam

patterning, the sample is developed in AR600-546 for 1min and rinsed in IPA. The e-beam patterns were etched through the SiN make layer by inductively coupled plasma (ICP, FAB star, CF_4 20sccm, CHF_3 30sccm, 4.0mTorr, RF1 150W, RF2 1000W, for 85sec) and the remaining e-beam resist layer was removed via AR600-71 remover for a few seconds. For etching a metal layer and MQW layer, the patterned SiN layer was used as a dry etch mask. The 55nm thick metal layer and 400nm thick MQW layer were etched via inductively coupled plasma (ICP, FAB star, Cl_2 45sccm, N_2 15sccm, 4.0mTorr, RF1 300W, RF2 2000W, for 53sec, selectivity of MQW, metal : SiN = 2:1.) and SiN mask was removed by wet etching with BOE solution. Figure 2.3.2 indicates sanning electron microscope (SEM) images of the fabricated metasurfaces.

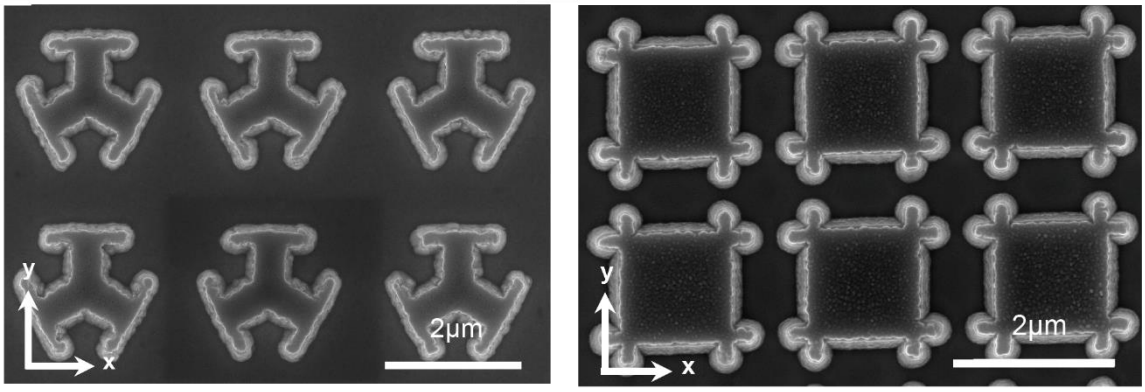

Figure 2.3.2. Scanning electron microscope (SEM) images of metasurfaces. (a) The top-view of the C3 structure for SHG and (b) C4 structure for THG.

2.4 Experiment

2.4.1 Intersubband absorption measurment

For optical characterization, spectrum of intersubband absorption from the MQW sample was measured via optical measurement setup in Figure 2.4.1. Figure 2.4.1 shows schematic of measurement setup for linear optical characterization. Unpolarized thermal light source from Fourier Transform Infrared Spectrometer (FTIR, Bruker Vertex 70) passes through a chopper and polarizer and converted to TM polarized light. In MQW case, only TM polarized light with an E-field component in the z-direction was absorbed by the intersubband transitions due to the MQW growth direction. The TM polarized light source passed in MQW sample several times, is then focused onto MCT detector. (Infrared Associate, Inc.). For this intersubband absorption measurement, a 2.52 mm long MQW sample piece was used. The both side of sample were polished to 45 degrees to form a multipath.

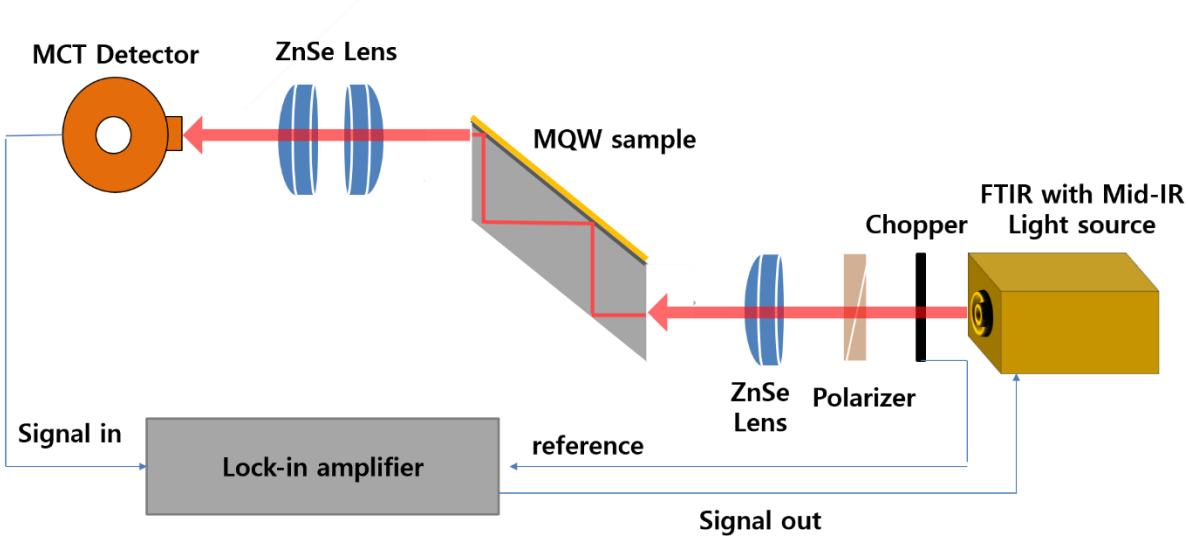

Figure 2.4.1. Measurement setup for linear optical characterization of the MQW. Thermal light source from the FTIR passes through a chopper, polarizer and is focused onto the MQW sample by a ZnSe lens. The light source passed in MQW sample several times, is then focused onto MCT detector.

Figure 2.4.2 shows the measured intersubband absorption spectrum. The intersubband transition energies were measured to be $E_{21} = \hbar\omega_{21} \approx 113 \ \ meV$, $E_{32} = \hbar\omega_{32} \approx 135 \ \ meV$,$E_{31} = \hbar\omega_{31} \approx 241 \ \ meV$,$E_{41} = \hbar\omega_{41} \approx 340 \ \ meV$, which matched well with the calculated values shown in Figure 2.2.1. The transition linewidths that were measured, were $2\hbar\gamma_{12} \approx 20.8 \ \ meV$, $2\hbar\gamma_{23} \approx 17.6 \ \ meV$, $2\hbar\gamma_{13} \approx 33.2 \ \ meV$, and $2\hbar\gamma_{14} \approx 43.6 \ \ meV$ for the 1–2, 2–3, 1–3, and 1–4 transitions, respectively. The intersubband absorption coefficients for each transition peak were calculated using

the formula provided in [Ref. 10] considering the sample geometry (length is 2.52 mm and thickness is 0.32 mm) where the thickness of the MQW layer was 390-nm-thick and the number of passes through the MQW layer was 3. The calculated intersubband absorption coefficients, α_W were 5.73 × 10^3 cm^{-1}, 2.06 × 10^3 cm^{-1}, 4.02 × 10^2 cm^{-1} and 2.60 × 10^2 cm^{-1} for the 1–2, 2–3, 1–3, and 1–4 transitions, respectively. The imaginary part of the out-of-plane dielectric constant of the MQW layer, $\varepsilon_\perp$ is directly connected to the α_W and it can be expressed as

$$\alpha_W = \frac{4\pi}{\lambda} Im(\sqrt{\varepsilon_\perp}) \tag{2.4.1}$$

$$\varepsilon_\perp(\omega) \approx \varepsilon_{core}(\omega) + \frac{e^2 N_e}{\varepsilon_0 \hbar}\left[\frac{z_{12}^2}{(\omega_{21}-\omega)-i\gamma_{21}} + \frac{z_{23}^2}{(\omega_{32}-\omega)-i\gamma_{32}} + \frac{z_{13}^2}{(\omega_{31}-\omega)-i\gamma_{31}} + \frac{z_{14}^2}{(\omega_{41}-\omega)-i\gamma_{41}}\right] \tag{2.4.2}$$

where ω indicates the pump frequency, ε_{core} indicates the averaged dielectric constant of the un-doped semiconductor, N_e is averaged volume doping density, e indicates the electron charge, and $\hbar\omega_{ij}$ is energy, $\hbar\gamma_{ij}$ is linewidth and z_{ij} is dipole moment, for the electron transition between subband i and j. The dielectric constant of the MQW for the in-plane E-field polarization ($\varepsilon_{\parallel}$) can be expressed by

$$\varepsilon_\parallel(\omega) \approx \varepsilon_{core}(\omega) + i\frac{N_e e^2 \tau_D}{\varepsilon_0 \omega m^*(1 - i\omega\tau_D)} \tag{2.4.3}$$

where $\tau_D \approx 10^{-13}s$ is the Drude relaxation time. Using the calculated dielectric constants of the MQW for the out-of-plane ($\varepsilon_\perp$) and in-plane ($\varepsilon_{\parallel}$) E-field polarizations, I inserted the designed MQW layer in the FDTD simulation.

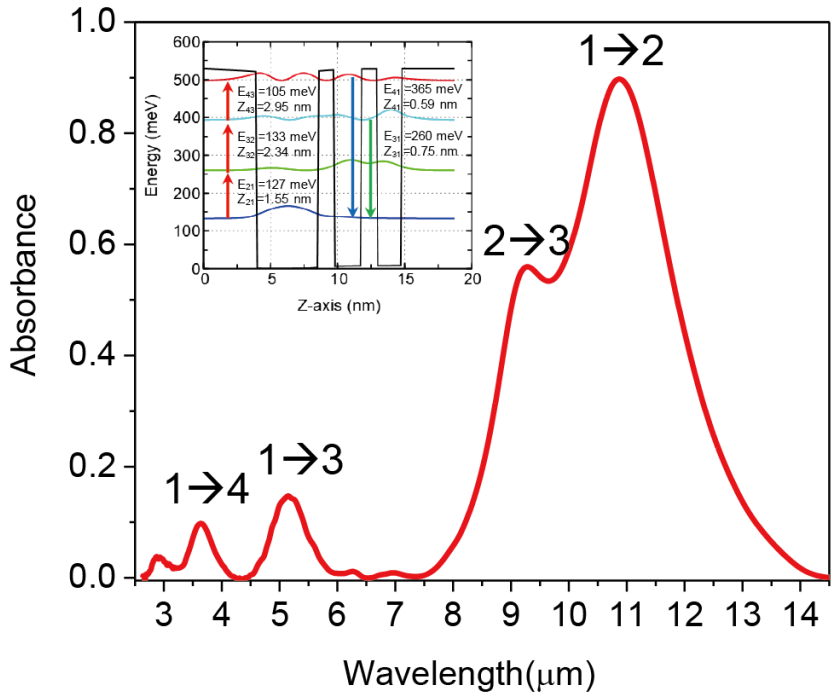

Figure 2.4.2. Measured intersubband absorption spectrum. The inset indicates the conduction band diagram for one period of our MQW layer.

2.4.2 Nonlinear Optical Characterization

Nonlinear optical measurements of the metasurface were measured via the nonlinear optical measurement setup shown in Figure. 2.4.3. Nonlinear metasurface samples were exposed by a quantum cascade laser (QCL, Daylight Solutions, Inc., Mircat system, tuning range: 909-1230 cm^{-1}, peak power output: 400 mW, repetition rate: 100 kHz, duty cycle: 10%) and a pulsed CO_2 laser (Coherent Inc., emission wavelength: 10.6 μm, peak power: 20 W, repetition rate: 20 MHz, duty cycle: 5%). A calibrated InSb photodetector (Electro Optical System Inc.), a long-pass (LP) filter used as a beam splitter, a SP filter used to block fundamental frequency (FF), input QWP (design wavelength: 9 μm), two different output QWPs (design wavelengths: 5 μm (for SHG) or 3 μm (for THG)), a collimating lens with a numerical aperture 0.85 (focal length: 1.87 mm) and ZnSe lens with a focal length : 3 inch were used to build the optical setup shown in Figure 2.4.3. The diameter of the input laser source that focused on the sample surface, was measured to be 2w = 12 μm by the knife-edge measurement.

Assuming Gaussian beam profiles, the intensity distributions of the input and output beams on the sample surface were expected as $I_{FF}e^{-2r^2/w^2}$ for the FF input pump, $I_{SH}e^{-4r^2/w^2}$ for the SHG output, and $I_{TH}e^{-6r^2/w^2}$ for the THG output.

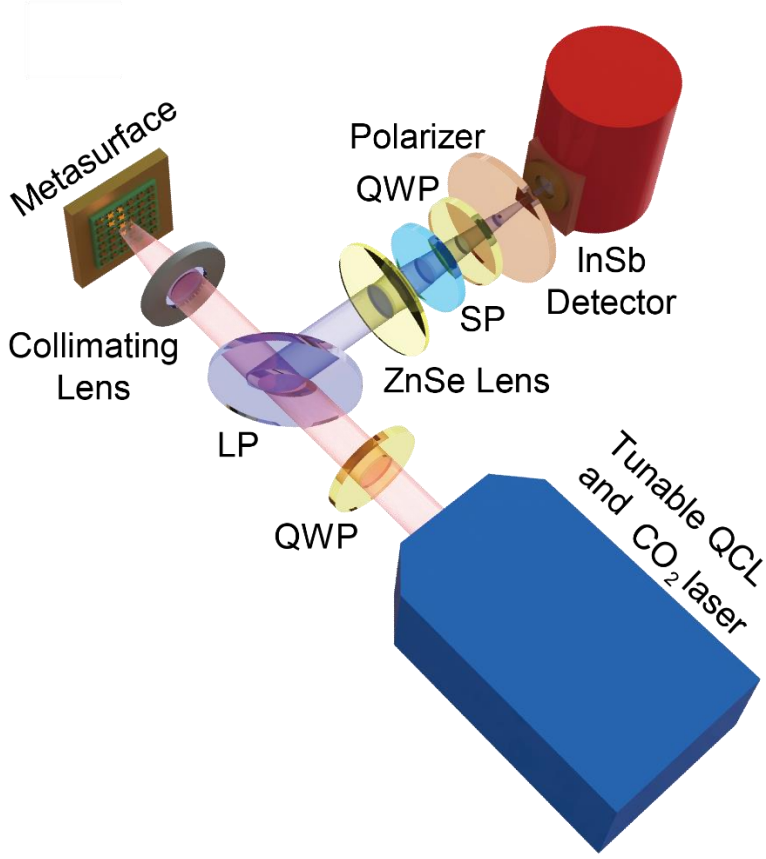

Figure 2.4.3. Schematic of measurement setup for nonlinear optical characterization. Light source from a tunable QCL and CO_2 laser passes through the quarter-wave plate (QWP) for circular polarization, a long pass filter (LP) to remove harmonic generation light coming from the laser and focused onto sample via numerical aperture 0.85 collimating lens. Nonlinear signal is collected by the collimating lens and is reflected by the LP towards the detector through a ZnSe lens, a short pass filter (SP) that is used as filter for blocking fundamental frequency, QWP and a polarizer. And then nonlinear signal is detected by the InSb detector.

Figure 2.4.4 a and b respectively show the experimental results of the SHG and THG signal peak power and intensity from the C3 and C4 metasurface as a function of the squared and cubed FF peak

power and peak intensity at a fixed emission wavelength of 10.5 μm of the QCL (Condition of the QCL : repetition rate: 100 kHz, duty cycle: 10%, current: 1300mA). In this nonlinear measurement, the RCP input pump beam was generated by QWP and the RCP SHG and RCP THG output signals were collected by using QWP and polarizer. To collect only RCP harmonic signal, the harmonic output signal is converted to a linearly polarized beam after the output QWP and its spin state (RCP or LCP) is analyzed by the linear polarizer. As shown in Figure 2.4.4, The SHG and THG peak powers of 0.35 μW and 0.17 μW were measured at the input peak intensity of only 80 kW cm^{-2} and at the input peak power of 45 mW. Input peak intensity and power were measured by power and energy meter (PM100D, Thorlabs) in front of the collimating lens.

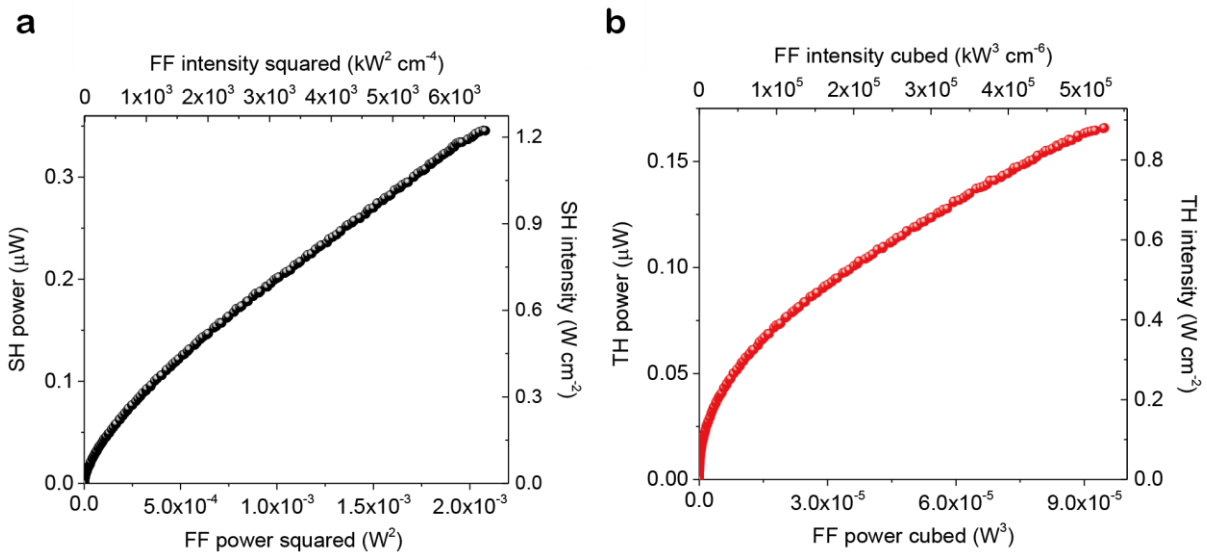

Figure 2.4.4. Nonlinear characterizations of SHG and THG metasurfaces. a,b) Nonlinear measurement results of SHG (black dot) and THG (red dot) peak power or intensity as a function of the FF input pump peak power squared and cubed or peak intensity squared and cubed for SHG and THG, respectively.

Figure 2.4.5 plots the experimental results of SHG (red dot) and THG (black dot) power conversion efficiencies at the wavelength of 10.5 μm. The power conversion efficiencies were calculated as

$$Input\ power\ /output\ power(mW)$$

(2.4.4)

$$\text{Output power} = \frac{(Lock\ in\ Voltage\ [mV] \times (10^{-4} InSb\ Responsivity\ \left[\frac{W}{V}\right])}{(InSb\ response) \times (ZnSe\ lens\ Transmittance)} \times \frac{1}{(SP\ filter\ Transmittance) \times (QWP\ Transmittance)} \quad (2.4.5)$$

where InSb response is 0.89, 0.63, ZnSe lens transmittance is 0.80, 0.79, SP filter transmittance is 0.8, 0.8, QWP transmittance is 0.93, 0.91 and InSb responsivity is 1/1.76, 1/1.76 for SHG (5.25 μm) and THG (3.5 μm), respectively.

I achieved 7.6×10^{-4} % and 3.6×10^{-4} % of power conversion efficiency for SHG and THG respectively, on the input pump power of 45 mW or pump intensity of 80 kW/cm. These values are three orders greater than the previously reported spin-controlled SHG metasurfaces.[45] The SHG power conversion efficiency in this result is comparable to the previously reported MQW loaded nonlinear metasurface results, and the THG power conversion efficiency is a record-high value for the same input pump intensity level.[10, 44, 46-47]

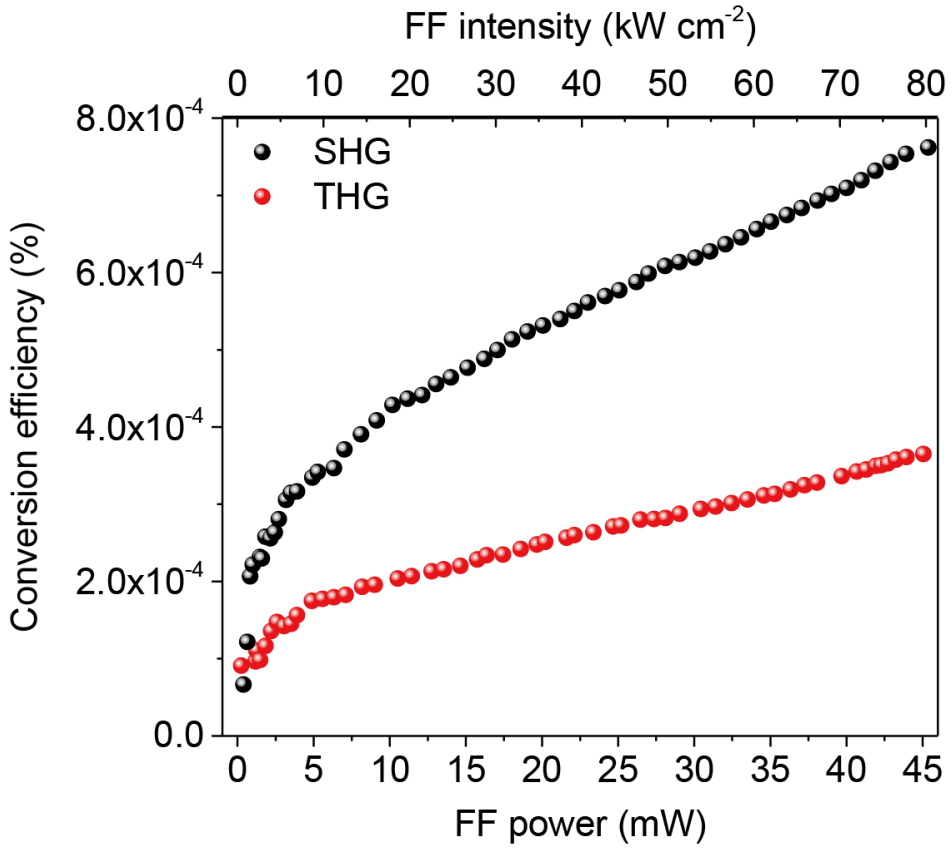

Figure 2.4.5. Nonlinear power conversion efficiencies of the SHG (black dot) and the THG (red dot) as functions of the FF peak power or intensity.

To confirm whether the spin state controlled nonlinear beam was generated by our metasurfaces, I analyzed the harmonic signals generated from the C3 and C4 metasurfaces based on the rotation of the output linear polarizer, and the results are presented in Figure 2.4.6 a and 2.4.6 b. In this measurement, the CO_2 laser (Coherent Inc., emission wavelength: 10.6 μm, peak power: 6~10 W, average power: 300~500Mw, repetition rate: 20 MHz, duty cycle: 5%) was used as an input pump to increase the signal contrast and ZnSe lens (focal length: 1/2 inch) was used for focusing input beam. In this measurement, the linearly polarized input beam from the CO_2 laser is converted to RCP through the QWP that located in front of the CO_2 laser, and the RCP input beam is focused onto metasurface via ZnSe lens and a harmonic signal is generated on the metasurface. The harmonic signal that generated from the metasurface is reflected by long pass filter and converted to a linear polarized beam through the QWP (Active wavelength: 5 μm for SHG case, 3 μm for THG case). In our case, angle of the polarizer indicate the spin state of the harmonic signal, that 0° and 180° indicate LCP and 90° indicates RCP (The direction of polarization can be changed by setting of the QWP). As shown in Figure 2.4.6, the measured harmonic signals were maximized at 90° and almost zero at 0° and 180° in both cases (SHG and THG). As the measured results, I can confirm the spin-state of the SHG and THG signals produced from the nonlinear metasurface, was accurately controlled by the spin-state of the input pump beam. As the results, the nonlinear metasurface that control the spin-states of SHG and THG simultaneously on the one-chip system based on the 2^{nd} and 3^{rd} order giant nonlinear responses of the MQW was well demonstrated.

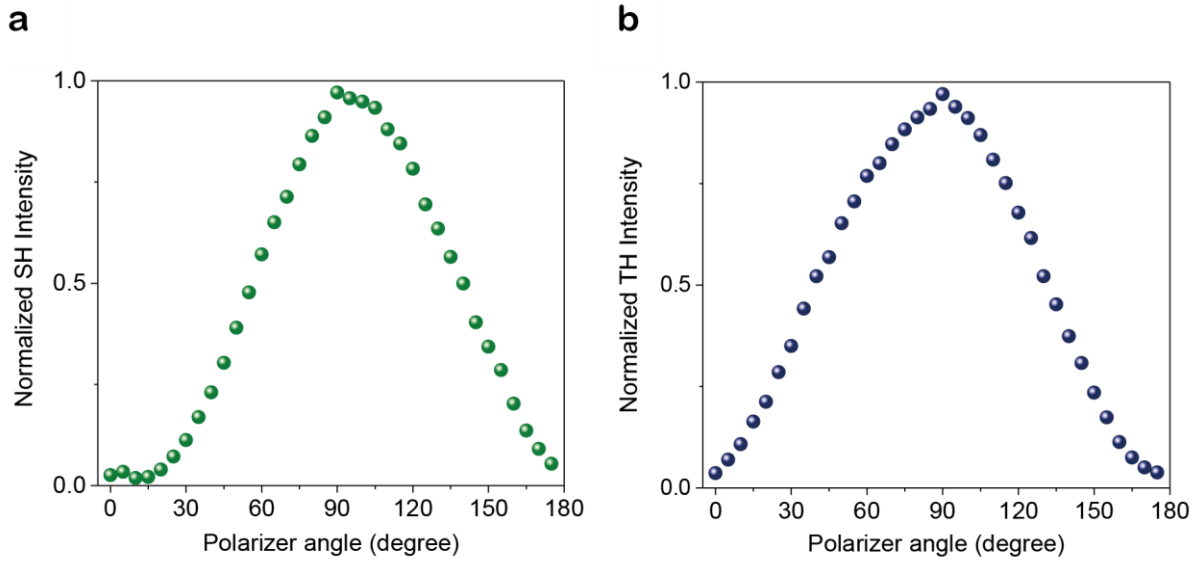

Figure 2.4.6. SHG (a) and THG (b) signals measured by varying the output polarizer angle at the RCP input pump beam. Polarizer angle of 0° and 180° represent a LCP harmonic signal and 90° represents a RCP harmonic signal for the RCP input pump beam.

2.4.3 Nonlinear Beam-steering Experiment

To provide the full potential of our nonlinear metasurface utilizing the continuously tunable local nonlinear phase, I demonstrated gradient metasurfaces for a nonlinear SHG and THG beam-steering. Based on the same C3 and C4 meta-atom structures that shown in Figure 2.4.7 a and b, I used C3 and C4 meta-atom structure with slightly different unit cell periods for changing rotation angle. The meta atom has the spatial variation of the orientation angle $\varphi(x, y)$ and the changes of the local phase of the nonlinear susceptibility are expressed as $\chi_{RRR}^{(2)eff}(x,y) = \chi_{RRR}^{(2)eff} e^{i3\varphi(x,y)}$ and $\chi_{RRRR}^{(3)eff}(x,y) = \chi_{RRRR}^{(3)eff} e^{i4\varphi(x,y)}$ for SHG and THG, respectively.

Figure 2.4.8 shows SEM images of the fabricated phase gradient arrays for SHG and THG beam-steering. The metasurfaces were fabricated with various rotational angles, $\Delta\varphi$, between adjacent meta-atoms and the $\Delta\varphi$ values equal to 20° and 30° for SHG (C3 structure, Figure 2.4.8 a and b), and 15° and 30° for THG (C4 structure, Figure 2.4.8 c and d).

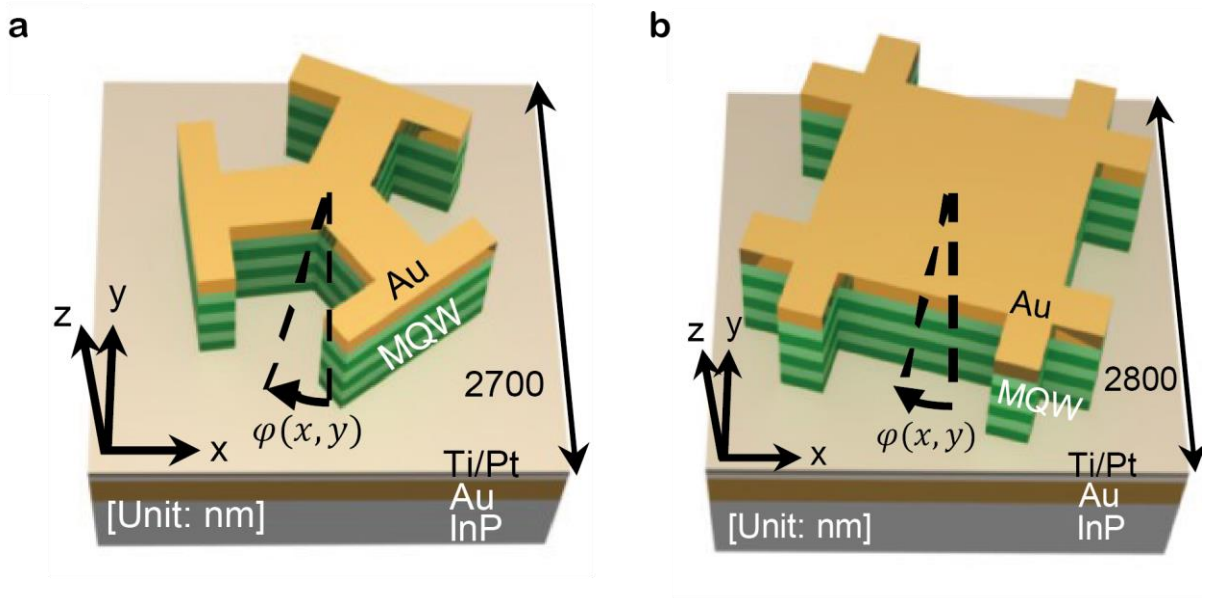

Figure 2.4.7. Schematic unit meta-atom structure for nonlinear beam-steering with C3 and C4 rotational symmetries for SHG (a) and THG (b), respectively. The spatial variation of the nano-structures orientation is indicated in the form of the angle φ

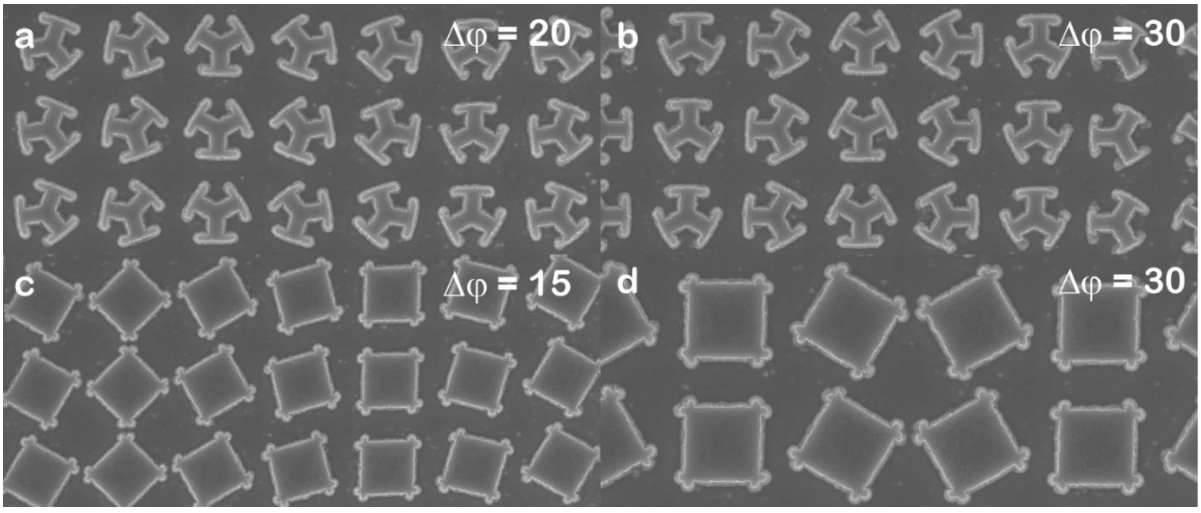

Figure 2.4.8. SEM images of the fabricated phase-gradient nonlinear metasurfaces with C3 and C4 structure. (a), (b) shows C3 structure for SHG with $\Delta\varphi$ equal to 20° and 30°, respectively. (c), (d) shows C4 structure for THG with $\Delta\varphi$ equal to 15° and 30°, respectively.

For the nonlinear beam-steering measurement, I used an optical set-up as shown in Figure 2.4.9 and the CO_2 laser (Coherent Inc., emission wavelength: 10.6 μm, peak power: 6~10 W, average power: 300~500Mw, repetition rate: 20 MHz, duty cycle: 5%) was used as an input pump and ZnSe lens (numerical aperture of 0.67, focal length: 1/2 inch, effective focal length: 10.2 mm) was used for focusing input beam. In this measurement, the linearly polarized input beam from the CO_2 laser is converted to RCP through the QWP that located in front of the CO_2 laser, and the RCP input beam is focused onto metasurface via ZnSe lens and a harmonic signal is generated. Unlike the nonlinear optical characterization set-up shown in Figure 2.4.3, in this measurement, the ZnSe lens that used as focusing harmonic signals onto detector, was removed. The harmonic signals that generated on the metasurface were collected by the same ZnSe lens and reached to the InSb detector directly through the SP, the QWP, and the polarizer. The RCP and LCP harmonic signals were selectively measured based on the adjustment of the polarizer as I mentioned before. As shown in Figure 2.4.9, the beam-steering angles of the harmonic signals were measured based on the measurement of the lateral shifts of the detector (d_{detector}). The lateral shift of the detector can be expressed as

$$d_{\text{detector}} = f \tan\theta \tag{2.4.6}$$

where f indicates the work distance of the lens (10.2 mm), and θ indicates the angle of the harmonic signal with respect to the normal beam path indicated in Figure 2.4.9. The beam-steering angle was measured by scanning with the InSb detector at 0.1 mm steps ($\Delta d_{\text{detector}}$ = 0.1 mm) in both positive and negative lateral directions, and the lateral shift distance was converted to an angle using equation 2.4.6.

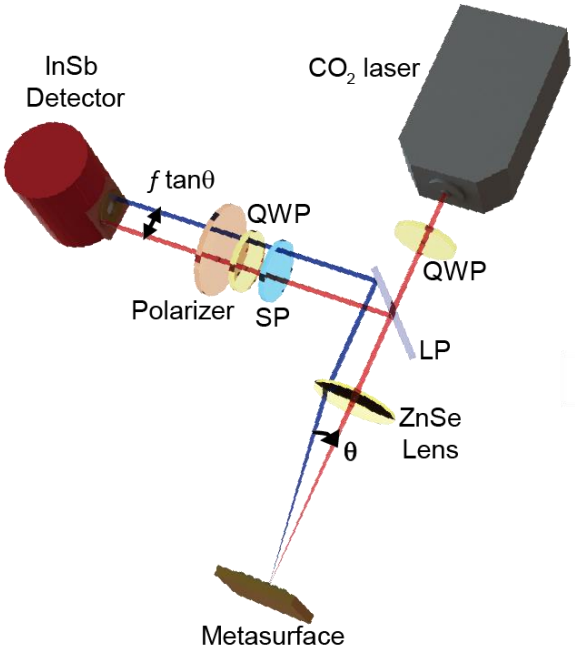

Figure 2.4.9. Optical measurement set-up for nonlinear beam-steering from phase-gradient nonlinear metasurface.

Figure 2.4.10 a and b show the measured far-field profiles of the SHG and THG output respectively, as a function of the beam-steering angle, which ranged from -35° to +35° and the range of the beam-steering angle was limited by radius of the ZnSe lens (beam steering angle limitation = $\tan^{-1}(radius\ of\ the\ \frac{lens}{effective}\ focal\ length)$). According to the basic reflect-array theory, in the case of the RCP input pump, the beam-steering angle with RCP component can be expressed as

$$\theta_{SH} = arcsin[(3\Delta\varphi/360°)\lambda_{SH}/d] \tag{2.4.7}$$

$$\theta_{TH} = arcsin[(4\Delta\varphi/360°)\lambda_{TH}/d] \tag{2.4.8}$$

for SHG and THG respectively, where *d* is the length of the periodic, as indicated in Figure 2.4.7 a and b. Following these equations, the beam-steering angle can be calculated to be equal to 18° and 28° in the case of the RCP SHG signal for $\Delta\varphi$ values equal to 20° and 30°, respectively, and 12° and 23° for the RCP THG signal for $\Delta\varphi$ values equal to 15° and 30°, respectively. In this measurement, the RCP input pump was used. The beam-steering angles of the RCP output signals with both SHG and the THG respectively generated from the C3 and C4 meta-atom-based gradient metasurfaces, matched very well with the theoretically calculated beam-steering angles indicated above. The harmonic LCP output signals were almost equal to zero and some peaks are generated due to the active wavelength of QWP (Input wavelength: 10.6 μm, SHG: 5.3 μm, THG: 3.5 μm and active wavelength of QWP: 9 μm, 5 μm, 3 μm) and fabrication error.

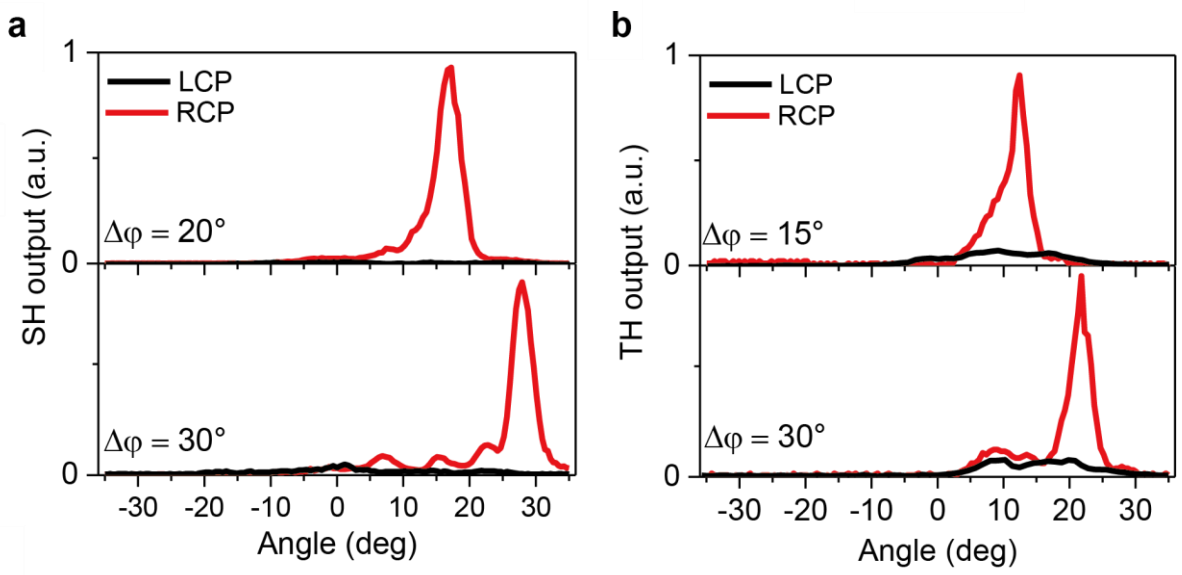

Figure 2.4.10. Far-field profiles of the beam-steering from the SHG (a) and THG (b) output from the phase-gradient nonlinear metasurfaces with $\Delta\varphi$ equal to 20° and 30° for SHG, and 15° and 30° for THG in the case of the RCP input pump. The black line represents a LCP output and the red line represents a RCP output for each harmonic signal.

2.5 Conclusion

I experimentally demonstrated one chip system with spin-controlled SHG and THG and nonlinear beam-steering as shown in Figure 2.5.1. The proposed approach will provide an efficient design platform for future applications based on nonlinear metasurfaces, such as nonlinear metasurface holography, nonlinear spectroscopy, nonlinear optical switching and modulation, and nonlinear information processing.

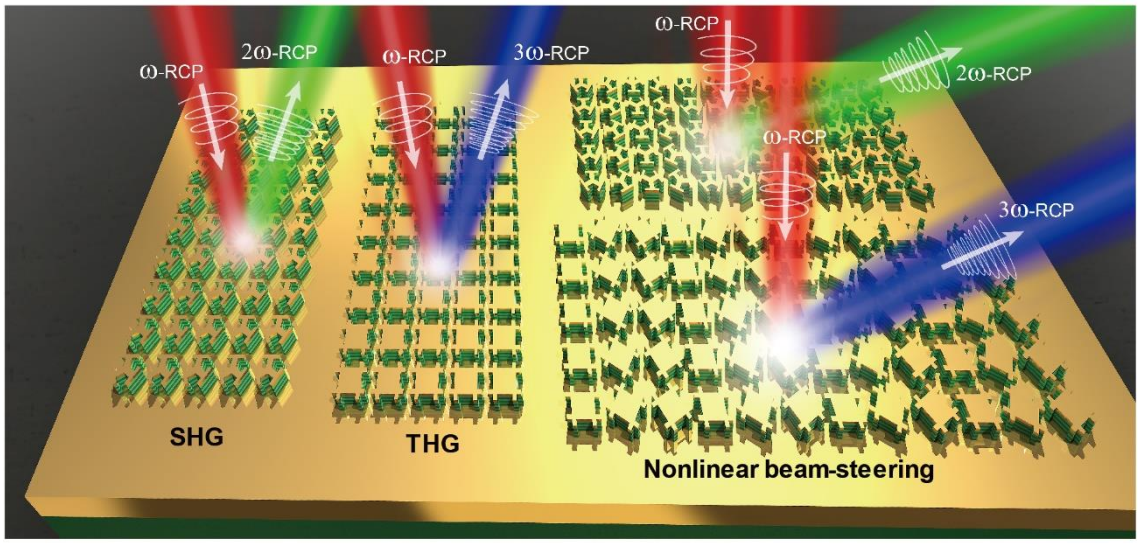

Figure 2.5.1. Schematic image of the concept of one chip system with spin-controlled SHG and THG and nonlinear beam-steering. Red, green, and blue beams indicate a input pump beam at the fundamental frequency (FF), a SHG beam, and a THG beam, respectively.

III. Outlook (Chiral nonlinear metasurface)

For our outlook study, I studied and demonstrated giant circular dichroism and spin-controlled harmonic generation for both SHG and THG using C3-chiral and C4-chiral structure, respectively. Figure 3.1.1 shows schematic of the concept of one chip system with spin-controlled and giant circular dichroism for SHG, THG and nonlinear beam-steering and unit cell designs. In this concept, for LCP input pump, only LCP-SHG signal is generated on the sample and for RCP input pump, only RCP-THG signal is generated on the sample.

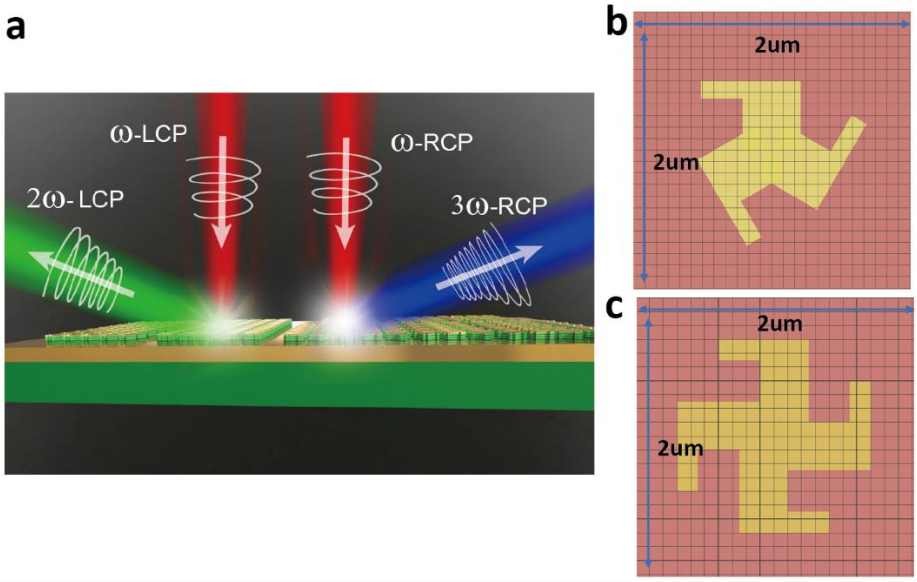

Figure 3.1.1. (a) Schematic of the concept of one chip system with spin-controlled and giant circular dichroism for both SHG and THG and nonlinear beam-steering. The red, green, and blue beams indicate an input pump beam at the fundamental frequency (FF), a SHG beam, and a THG beam, respectively. (b, c) Schematics of unit meta-atom structure with C3-chiral designed for SHG and unit meta-atom structure with C4-chiral designed for THG

Figure 3.1.2 shows the E_z field distributions on the plasmonic resonator. The E_z field distributions were monitored in the MQW layer (below 100nm in Au layer) and LCP input pump and RCP input pump were used as input source (wavelength: 10.5 μm). In RCP input pump case, as shown in Figure 3.1.2, the FF E_z field and HF E_z field are well overlapping each other (Simulated overlap factor: 1.33352, simulated by FDTD simulation). However, in LCP input case, the HF E_z fields indicated black circles in Figure 3.1.3 are weaker than RCP input case. Therefore, the FF E_z field and HF E_z field do not overlap well (Simulated overlap factor: 0.056357, simulated by FDTD simulation). As I mentioned in Chapter 2.2.1, the relation expression between SH, TH peak power and overlap factor can be expressed as

$$\text{SH, TH peak power} \propto (\text{overlap factor})^2 \tag{3.1.1}$$

Therefore, in this case, harmonic peak power with RCP input is 400 magnitude higher than harmonic peak power with LCP input.

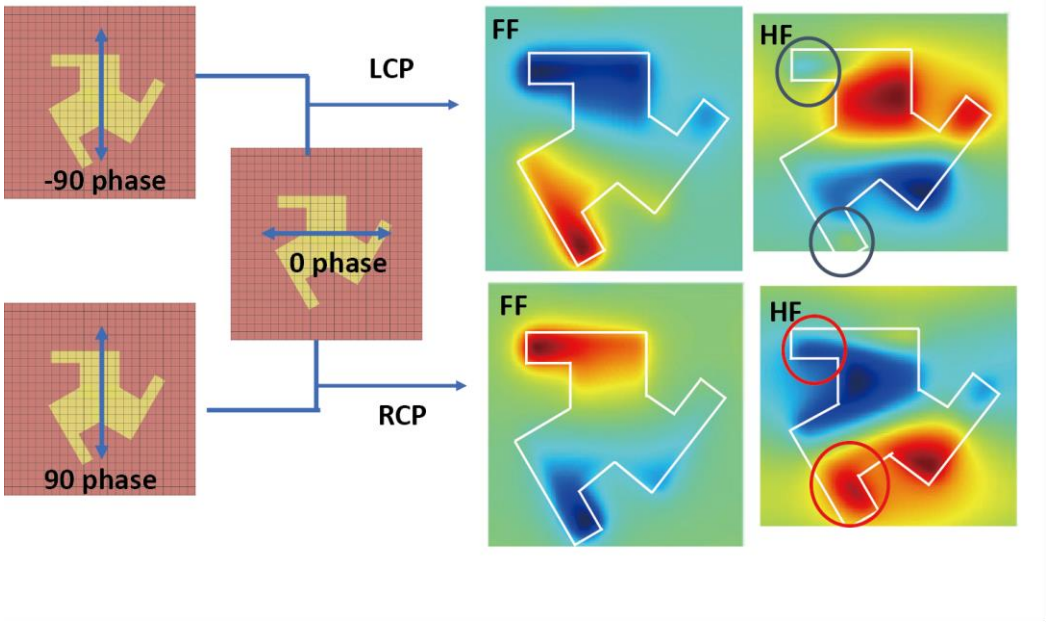

Figure 3.1.2. The normalized E_z field distribution on the plasmonic. The E_z field monitor is in MQW layer. Top-view cross-section at the 10.5 μm (FF) and 5.25 μm (SH) for the C3 meta-atom. In RCP case,

the red circles indicate strong HF E_z field that can be overlapped with FF E_z field In LCP case, the black circles indicate disappearance of the HF E_z field.

Figure 3.1.3 shows simulation and measurement results of the SHG circular dichroism (CD) and THG-CD from the C3-chiral and C4-chiral plasmonic nanostructure. As shown in Figure 3.1.3, measured SHG-CD is matched well with simulation result, however measured THG-CD is not matched well with simulation result. I will make an effort to optimize the C4-chiral plasmonic nanostructure and fabricate the nonlinear beam-steering using nonlinear gradient metasurface with C3-chiral and C4-chiral plasmonic nanostructure.

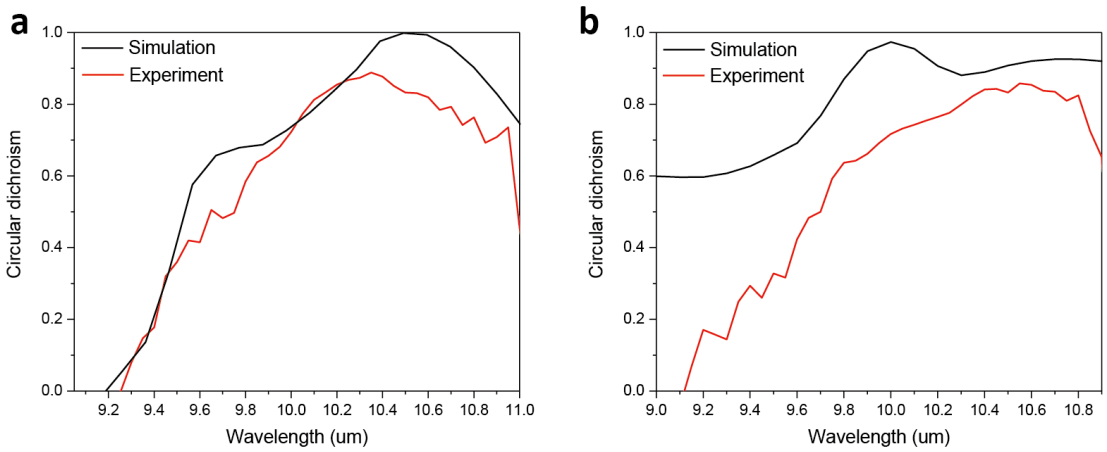

Figure 3.1.3. Simulation and measurement results of the SHG circular dichroism (CD) (a) and THG-CD (b) from the C3- chiral and C4- chiral plasmonic nanostructure. The black lines indicate simulation result and the red lines indicate measurement result.

IV. Conclusion

4.1 Summary

In this dissertation, I discussed spin-state controlled nonlinear metasurface and giant circular dichroism nonlinear metasurface with giant nonlinear response. As shown in Chapter 2, I successfully demonstrated the implementation of a novel class of a nonlinear metasurface platform based on the combination of the quantum-engineered MQW structure. Using plasmonic nanoantennas with C3 or C4 rotational symmetry structure I experimentally demonstrated nonlinear metasurface that designed to produce giant 2^{nd} and 3^{rd} order nonlinear responses simultaneously and to control the spin-state of nonlinear response. The SHG and THG far-field are produced efficiently on the same chip selectively or simultaneously, depending on the shape of the plasmonic nanoantenna. In Chapter 3, I discussed a novel implementation of chiral plasmonic metasurface with giant nonlinear circular dichroism for both SHG and THG on one-chip system. I experimentally demonstrated the giant nonlinear circular dichroism for both SHG and THG on one-chip at wide wavelength region.

For future works, I develop the chiral plasmonic metasurface and design the electrical tuning metasurface for changing the peak position of the nonlinear signal.

REFERENCES

1. Almeida, E.; Bitton, O.; Prior, Y., Nonlinear metamaterials for holography. *Nature Communications* **2016,** *7*, 12533.
2. Maier, S., Plasmonics: Fundamentals and Applications (Springer, Berlin, 2007).
3. Raether, H., Surface plasmons on smooth surfaces. In *Surface plasmons on smooth and rough surfaces and on gratings*, Springer: 1988; pp 4-39.
4. Mueller, G., *Intersubband Transitions in Quantum Wells: Physics and Device Applications II*. Academic Press: 1999; Vol. 66.
5. Yanagi, K.; Okada, R.; Ichinose, Y.; Yomogida, Y.; Katsutani, F.; Gao, W.; Kono, J., Intersubband plasmons in the quantum limit in gated and aligned carbon nanotubes. *Nature communications* **2018,** *9* (1), 1121.
6. Capasso, F.; Sirtori, C.; Cho, A. Y., Coupled quantum well semiconductors with giant electric field tunable nonlinear optical properties in the infrared. *IEEE Journal of Quantum Electronics* **1994,** *30* (5), 1313-1326.
7. Rosencher, E.; Bois, P.; Nagle, J.; Delaitre, S., Second harmonic generation by intersub-band transitions in compositionally asymmetrical MQWs. *Electronics Letters* **1989,** *25* (16), 1063-1065.
8. Sirtori, C.; Capasso, F.; Sivco, D. L.; Chu, S.; Cho, A. Y., Observation of large second order susceptibility via intersubband transitions at $\lambda\sim$ 10 μm in asymmetric coupled AlInAs/GaInAs quantum wells. *Applied physics letters* **1991,** *59* (18), 2302-2304.
9. Yoo, S.; Fejer, M.; Byer, R.; Harris Jr, J., Second-order susceptibility in asymmetric quantum wells and its control by proton bombardment. *Applied physics letters* **1991,** *58* (16), 1724-1726.
10. Yu, J.; Park, S.; Hwang, I.; Kim, D.; Jung, J. Y.; Lee, J., Third-Harmonic Generation from Plasmonic Metasurfaces Coupled to Intersubband Transitions. *Advanced Optical Materials* **2019,** *7* (9), 1801510.
11. Gravé, I.; Segev, M.; Yariv, A., Observation of phase conjugation at 10.6 μm via intersubband third-order nonlinearities in a GaAs/AlGaAs multi-quantum-well structure. *Applied physics letters* **1992,** *60* (22), 2717-2719.
12. Sa'ar, A.; Kuze, N.; Feng, J.; Grave, I.; Yariv, A., Observation of third-order intersubband dc Kerr effect at the midinfrared wavelengths in GaAs quantum wells. *Applied physics letters* **1992,** *61* (11), 1263-1265.
13. Walrod, D.; Auyang, S.; Wolff, P.; Sugimoto, M., Observation of third order optical nonlinearity due to intersubband transitions in AlGaAs/GaAs superlattices. *Applied physics letters* **1991,** *59* (23), 2932-2934.

14. Weber, E. R.; Willardson, R. K.; Liu, H.; Capasso, F., *Intersubband transitions in quantum wells: physics and device applications*. Academic press: 1999; Vol. 62.

15. Li, G.; Zhang, S.; Zentgraf, T., Nonlinear photonic metasurfaces. *Nature Reviews Materials* **2017,** *2* (5), 17010.

16. Fejer, M. M.; Magel, G.; Jundt, D. H.; Byer, R. L., Quasi-phase-matched second harmonic generation: tuning and tolerances. *IEEE Journal of Quantum Electronics* **1992,** *28* (11), 2631-2654.

17. Patel, C.; Van Tran, N., PHASE-MATCHED NONLINEAR INTERACTION BETWEEN CIRCULARLY POLARIZED WAVES. *Applied Physics Letters* **1969,** *15* (6), 189-191.

18. Rose, A.; Huang, D.; Smith, D. R., Nonlinear interference and unidirectional wave mixing in metamaterials. *Physical review letters* **2013,** *110* (6), 063901.

19. Zheludev, N.; Emel'yanov, V., Phase matched second harmonic generation from nanostructured metallic surfaces. *Journal of Optics A: Pure and Applied Optics* **2003,** *6* (1), 26.

20. Zhu, S.-n.; Zhu, Y.-y.; Qin, Y.-q.; Wang, H.-f.; Ge, C.-z.; Ming, N.-b., Experimental Realization of Second Harmonic Generation in a Fibonacci Optical Superlattice of LiTa O 3. *Physical review letters* **1997,** *78* (14), 2752.

21. Boyd, R.; Masters, B., Nonlinear Optics 3rd edn (New York: Academic). **2008**.

22. Shen, Y.-R., The principles of nonlinear optics. *New York, Wiley-Interscience, 1984, 575 p.* **1984**.

23. Bomzon, Z. e.; Biener, G.; Kleiner, V.; Hasman, E., Space-variant Pancharatnam–Berry phase optical elements with computer-generated subwavelength gratings. *Optics letters* **2002,** *27* (13), 1141-1143.

24. Chen, S.; Cai, Y.; Li, G.; Zhang, S.; Cheah, K. W., Geometric metasurface fork gratings for vortex-beam generation and manipulation. *Laser & Photonics Reviews* **2016,** *10* (2), 322-326.

25. Khorasaninejad, M.; Chen, W. T.; Devlin, R. C.; Oh, J.; Zhu, A. Y.; Capasso, F., Metalenses at visible wavelengths: Diffraction-limited focusing and subwavelength resolution imaging. *Science* **2016,** *352* (6290), 1190-1194.

26. Maguid, E.; Yulevich, I.; Veksler, D.; Kleiner, V.; Brongersma, M. L.; Hasman, E., Photonic spin-controlled multifunctional shared-aperture antenna array. *Science* **2016,** *352* (6290), 1202-1206.

27. Pancharatnam, S. In *Generalized theory of interference and its applications*, Proceedings of the Indian Academy of Sciences-Section A, Springer: 1956; pp 398-417.

28. Li, G. X.; Chen, S. M.; Pholchai, N.; Reineke, B.; Wong, P. W. H.; Pun, E. Y. B.; Cheah, K. W.; Zentgraf, T.; Zhang, S., Continuous control of the nonlinearity phase for harmonic generations. *Nature Materials* **2015,** *14* (6), 607-612.

29. Nookala, N.; Lee, J.; Tymchenko, M.; Gomez-Diaz, J. S.; Demmerle, F.; Boehm, G.; Lai, K. F.; Shvets, G.; Amann, M. C.; Alu, A.; Belkin, M., Ultrathin gradient nonlinear metasurface with a giant nonlinear response. *Optica* **2016,** *3* (3), 283-288.

30. Schlickriede, C.; Waterman, N.; Reineke, B.; Georgi, P.; Li, G. X.; Zhang, S.; Zentgraf, T., Imaging through Nonlinear Metalens Using Second Harmonic Generation. *Advanced Materials* **2018,** *30* (8), 1703843.

31. Segal, N.; Keren-Zur, S.; Hendler, N.; Ellenbogen, T., Controlling light with metamaterial-based nonlinear photonic crystals. *Nature Photonics* **2015,** *9* (3), 180-184.

32. Tymchenko, M.; Gomez-Diaz, J. S.; Lee, J.; Nookala, N.; Belkin, M. A.; Alu, A., Gradient Nonlinear Pancharatnam-Berry Metasurfaces. *Physical Review Letters* **2015,** *115* (20), 207403.

33. Ye, W. M.; Zeuner, F.; Li, X.; Reineke, B.; He, S.; Qiu, C. W.; Liu, J.; Wang, Y. T.; Zhang, S.; Zentgraf, T., Spin and wavelength multiplexed nonlinear metasurface holography. *Nature Communications* **2016,** *7*, 11930.

34. Keren-Zur, S.; Avayu, O.; Michaeli, L.; Ellenbogen, T., Nonlinear beam shaping with plasmonic metasurfaces. *ACS Photonics* **2015,** *3* (1), 117-123.

35. Ye, W.; Zeuner, F.; Li, X.; Reineke, B.; He, S.; Qiu, C.-W.; Liu, J.; Wang, Y.; Zhang, S.; Zentgraf, T., Spin and wavelength multiplexed nonlinear metasurface holography. *Nature communications* **2016,** *7*, 11930.

36. Berry, M. V., Quantal phase factors accompanying adiabatic changes. *Proceedings of the Royal Society of London. A. Mathematical and Physical Sciences* **1984,** *392* (1802), 45-57.

37. Li, G.; Chen, S.; Pholchai, N.; Reineke, B.; Wong, P. W. H.; Pun, E. Y. B.; Cheah, K. W.; Zentgraf, T.; Zhang, S., Continuous control of the nonlinearity phase for harmonic generations. *Nature materials* **2015,** *14* (6), 607.

38. Bhagavantam, S.; Chandrasekhar, P. In *Harmonic generation and selection rules in nonlinear optics*, Proceedings of the Indian Academy of Sciences-Section A, Springer: 1972; pp 13-20.

39. Burns, W.; Bloembergen, N., Third-harmonic generation in absorbing media of cubic or isotropic symmetry. *Physical Review B* **1971,** *4* (10), 3437.

40. Chen, S.; Li, G.; Zeuner, F.; Wong, W. H.; Pun, E. Y. B.; Zentgraf, T.; Cheah, K. W.; Zhang, S., Symmetry-selective third-harmonic generation from plasmonic metacrystals. *Physical review letters* **2014,** *113* (3), 033901.

41. Konishi, K.; Higuchi, T.; Li, J.; Larsson, J.; Ishii, S.; Kuwata-Gonokami, M., Polarization-controlled circular second-harmonic generation from metal hole arrays with threefold rotational symmetry. *Physical review letters* **2014,** *112* (13), 135502.

42. Chen, H. T.; Taylor, A. J.; Yu, N. F., A review of metasurfaces: physics and applications. *Reports on Progress in Physics* **2016,** *79* (7), 076401.

43. Yu, N. F.; Capasso, F., Flat optics with designer metasurfaces. *Nature Materials* **2014,** *13* (2), 139-150.

44. Lee, J.; Tymchenko, M.; Argyropoulos, C.; Chen, P. Y.; Lu, F.; Demmerle, F.; Boehm, G.; Amann, M. C.; Alu, A.; Belkin, M. A., Giant nonlinear response from plasmonic metasurfaces coupled to intersubband transitions. *Nature* **2014,** *511* (7507), 65-69.

45. Li, G. X.; Wu, L.; Li, K. F.; Chen, S. M.; Schlickriede, C.; Xu, Z. J.; Huang, S. Y.; Li, W. D.; Liu, Y. J.; Pun, E. Y. B.; Zentgraf, T.; Cheah, K. W.; Luo, Y.; Zhang, S., Nonlinear Metasurface for Simultaneous Control of Spin and Orbital Angular Momentum in Second Harmonic Generation. *Nano Letters* **2017,** *17* (12), 7974-7979.

46. Huang, L. L.; Chen, X. Z.; Muhlenbernd, H.; Zhang, H.; Chen, S. M.; Bai, B. F.; Tan, Q. F.; Jin, G. F.; Cheah, K. W.; Qiu, C. W.; Li, J. S.; Zentgraf, T.; Zhang, S., Three-dimensional optical holography using a plasmonic metasurface. *Nature Communications* **2013,** *4*, 2808.

47. Lee, J.; Nookala, N.; Gomez-Diaz, J. S.; Tymchenko, M.; Demmerle, F.; Boehm, G.; Amann, M. C.; Alu, A.; Belkin, M. A., Ultrathin Second-Harmonic Metasurfaces with Record-High Nonlinear Optical Response. *Advanced Optical Materials* **2016,** *4* (5), 664-670.